

AD \_\_\_\_\_

AWARD NUMBER: W81XWH-07-1-0640

TITLE: Acoustic Inverse Scattering for Breast Cancer Microcalcification Detection

PRINCIPAL INVESTIGATOR: Matthew A. Lewis, Ph.D.

CONTRACTING ORGANIZATION: University of Texas Southwestern Medical Center  
at Dallas  
Dallas, TX 75390

REPORT DATE: September 2009

TYPE OF REPORT: Annual

PREPARED FOR: U.S. Army Medical Research and Materiel Command  
Fort Detrick, Maryland 21702-5012

DISTRIBUTION STATEMENT: Approved for Public Release;  
Distribution Unlimited

The views, opinions and/or findings contained in this report are those of the author(s) and should not be construed as an official Department of the Army position, policy or decision unless so designated by other documentation.

# REPORT DOCUMENTATION PAGE

Form Approved  
OMB No. 0704-0188

Public reporting burden for this collection of information is estimated to average 1 hour per response, including the time for reviewing instructions, searching existing data sources, gathering and maintaining the data needed, and completing and reviewing this collection of information. Send comments regarding this burden estimate or any other aspect of this collection of information, including suggestions for reducing this burden to Department of Defense, Washington Headquarters Services, Directorate for Information Operations and Reports (0704-0188), 1215 Jefferson Davis Highway, Suite 1204, Arlington, VA 22202-4302. Respondents should be aware that notwithstanding any other provision of law, no person shall be subject to any penalty for failing to comply with a collection of information if it does not display a currently valid OMB control number. PLEASE DO NOT RETURN YOUR FORM TO THE ABOVE ADDRESS.

1. REPORT DATE 1 September 2009	2. REPORT TYPE Annual	3. DATES COVERED 17 Aug 2008 – 16 Aug 2009		
4. TITLE AND SUBTITLE  Acoustic Inverse Scattering for Breast Cancer Microcalcification Detection		5a. CONTRACT NUMBER		
		5b. GRANT NUMBER W81XWH-07-1-0640		
		5c. PROGRAM ELEMENT NUMBER		
6. AUTHOR(S)  Matthew A. Lewis, Ph.D.  E-Mail: matthew.lewis@utsouthwestern.edu		5d. PROJECT NUMBER		
		5e. TASK NUMBER		
		5f. WORK UNIT NUMBER		
7. PERFORMING ORGANIZATION NAME(S) AND ADDRESS(ES)  University of Texas Southwestern Medical Center at Dallas Dallas, TX 75390		8. PERFORMING ORGANIZATION REPORT NUMBER		
9. SPONSORING / MONITORING AGENCY NAME(S) AND ADDRESS(ES) U.S. Army Medical Research and Materiel Command Fort Detrick, Maryland 21702-5012		10. SPONSOR/MONITOR'S ACRONYM(S)		
		11. SPONSOR/MONITOR'S REPORT NUMBER(S)		
12. DISTRIBUTION / AVAILABILITY STATEMENT Approved for Public Release; Distribution Unlimited				
13. SUPPLEMENTARY NOTES				
14. ABSTRACT An advanced scalar inverse scattering theory developed by Colton, Kirsch, and others in the inverse scattering community can determine the shape of scatterers with size on the order of the wavelength. In addition to size and number, the morphology of breast microcalcifications is an important diagnostic indicator. Our hypothesis is that the linear sampling method (LS), when augmented with a method for estimating the inhomogeneous Green's function for wave propagation in the breast, can be translated to an acoustic imaging system to detect, localize, and characterize microcalcifications in breast phantoms using data from the far-field scattering measurements. Progress continues on developing an appropriate estimator of the background Green's function from scattering data, and a phantom with hard, extended scatterers has been developed for proof-of-concept. Data acquisition and analysis is on-going, with one peer-reviewed conference proceedings paper in past year.				
15. SUBJECT TERMS ultrasound, inverse scattering, optimum array processing, breast cancer screening, detection, estimation, linear sampling method				
16. SECURITY CLASSIFICATION OF:  a. REPORT U		17. LIMITATION OF ABSTRACT UU	18. NUMBER OF PAGES 34	19a. NAME OF RESPONSIBLE PERSON USAMRMC
b. ABSTRACT U				19b. TELEPHONE NUMBER (include area code)
c. THIS PAGE U				

## **Table of Contents**

	<u>Page</u>
<b>Introduction.....</b>	<b>4</b>
<b>Body.....</b>	<b>4</b>
<b>Key Research Accomplishments.....</b>	<b>6</b>
<b>Reportable Outcomes.....</b>	<b>6</b>
<b>Conclusion.....</b>	<b>6</b>
<b>References.....</b>	<b>6</b>
<b>Appendices.....</b>	<b>7-34</b>

# 1 Introduction

Microcalcification detection is the hallmark of mammography as a breast cancer screening modality. For technical reasons, ultrasonic detection of all mammographically-visible microcalcifications has been problematic. In clinical ultrasound, high frequencies must be used to resolve microcalcifications below 200 micrometers. Unfortunately, ultrasonics above 10 MHz suffer from appreciable attenuation in soft tissues, and depth of penetration is limited. Transmission diffraction tomography, while well-suited for the geometry of the breast, is inherently insensitive to scattering caused by small, hard inhomogeneities. A more general form of acoustic inverse scattering is therefore needed for microcalcification detection and localization by ultrasound. We find rationale in the advanced scalar inverse scattering theory developed by Colton, Kirsch, and others in the RADAR community that can determine the shape of scatterers with size on the order of the wavelength. In addition to size and number, the morphology of breast microcalcifications is an important diagnostic indicator. Our hypothesis is that the linear sampling method (LS), when augmented with a method for estimating the inhomogeneous Green's function for wave propagation in the breast, can be translated to an acoustic imaging system to detect, localize, and characterize microcalcifications in breast phantoms using data from the scattering measurements in a tomographic geometry.

# 2 Body

The goal of this research endeavor is to develop a bistatic ultrasound imaging method that specifically targets breast microcalcifications. By bistatic imaging, we mean that receiver and transmitter can be separated in space. Since there are several commercial breast acoustic tomography systems currently undergoing FDA trials, we believe that it is the appropriate time to apply state-of-the-art methods from optimum array processing and inverse scattering to this important biomedical imaging problem.

In year 2 of this research, the majority of our efforts have focused on development of a microcalcification detection algorithm that incorporated *a priori* information on soft tissue inhomogeneities and experimentation in phantoms to demonstrate the potential of the proposed method. In Task 6 of the original Statement of Work, we have continued our research into developing an elliptical Radon-based approach to imaging the heterogeneous background Green's function. As reported in year 1, the published work of a French group [1] is clearly incorrect since it does not reproduce the known results for spherical Radon transform in the limiting case. The applied mathematicians supported under this Synergistic Idea award have made significant progress in analyzing this model, and a paper on this work is expected to be submitted in the proposed no-cost extension period. In summary, we have found some success in diagonalizing the elliptical Radon transform in a manner that produces a series-based inversion. The coefficients in this reconstruction algorithm are given by integral equations that can be solved numerically. Current efforts by collaborators at UT Arlington are in the direction of efficiently implementing this inversion as a numerical method that can be trans-

lated to the prototype system at UT Southwestern. For a further review by collaborators on the sub-award, please see the attached Appendix A.

The second major effort for year 2 of this research project was imaging experiments with phantoms and simulated microcalcifications. Six high signal-to-noise multi-static response matrix data sets were acquired. These data supplement the scattering data from wires obtained in year 1 (so-called point scatterers), and include metal scatterers with both circular, hexagonal, and star cross sections. The strong scatterers were embedded in a 7 cm diameter gelatin cylinder with known acoustic properties. Image reconstruction and data analysis for these data sets is on-going and will be submitted for publication in the proposed no-cost extension period. In addition, since June 2009 we have been investigating more sophisticated phantoms for validation. In one case, water-filled voids are introduced into the gelatin to produce a heterogeneous background. Fluctuations in the data due to these heterogeneities can be similar in appearance to the signals due to the strong scatterer. In a parallel development to support Task 7 (statistical characterization of speckle noise and suppression methods), we have experimented with phantoms with clutter to produce the type of speckle observed in real soft tissue. We have adopted a method from the literature[2], and have confirmed the B-mode appearance of this phantom using a VisualSonics Vevo700 small animal ultrasound system. In the proposed no-cost extension period, additional data acquisition experiments will be performed as a part of Task 7 where hard 2D scatterers will be included in phantom. We anticipate completion of these experiments in the next year with the goal of understanding the effect of speckle noise on the the robustness of the linear sampling method for estimating microcalcification morphology.

For Task 13, a peer-reviewed conference proceeding publication[3] was printed in early 2009 (see Appendix B). This work was in support of Tasks 6 and 12, and was made possible by the support of a Biomedical Engineering graduate student through this research project. In addition, a collaborator supported under the sub-award published a peer-reviewed book chapter on acoustic tomography in breast imaging. His support under this research project was critical to the completion of this, and it is noted in the acknowledgements of the publication[4]. At present, the BME graduate student and PI at UT Southwestern are preparing an expanded publication on bistatic ultrasound imaging of scatterers in the breast for an IEEE transactions, and a supported graduate student in Mathematics and collaborators at UT Arlington anticipate at least 2 submitted publications in the proposed no-cost extension period.

In the next year, we anticipate completion of the image reconstruction and data analysis tasks, along with some additional experiments to test the robustness of the described methods to sub-wavelength scatter. In the proposed no-cost extension period, support will continue for graduate students at UT Southwestern and UT Arlington, while the PI and collaborators will continue the Statement of Work research through departmental cost sharing.

### **3 Key Research Accomplishments**

- Data collection of six 2D phantoms with materials mimicking breast tissues and microcalcifications.
- Development of elliptical Radon transform model for bistatic estimation of background Green's function.
- Identification of fundamental shortcoming in the breast ultrasound tomography literature as it relates to bistatic imaging, and the development of an iterative approach for estimating the inhomogeneous background in the inverse scattering problem.

### **4 Reportable Outcomes**

- A publication on ultrasound tomography using the elliptical Radon transform model[3].
- A review article on tomographic imaging using spherical Radon transform models[4].
- Two collaborators (M Lewis and G Ambartsoumian) participated in the 2008 NSF/CBMS Rice Workshop on Imaging in Random Media, where image reconstructions methods of the types of interest in this research study were the focus.

### **5 Conclusion**

We have maintained a reasonable focus with our original Statement of Work. We self-identify delayed progress on Task 12 (Image reconstruction and data analysis) which will be remedied by ongoing work in the no-cost extension period. In addition, further experiments and data acquisition using more complicated phantoms will facilitate extensions of Tasks 7 and 11. We anticipate that successful completion of Task 12 will produce multiple additional publications that will support translation of these image reconstruction methods to a commercial breast ultrasound tomography system. In the coming year, we will actively solicit research collaborations in this area.

### **References**

- [1] Serge Mensah and Emile Franceschini. Near-field ultrasound tomography. *JASA*, 121(3):1423, 2007.
- [2] Helen Morehouse, Harshada Pranav Thaker, and Chandowti Persaud. Addition of metamucil to gelatin for a realistic breast biopsy phantom. *J Ultrasound Med*, 26:1123–1126, 2007.

- [3] Ravi Skankar Vaidyanathan, Matthew A. Lewis, Gaik Ambartsoumian, and Tuncay Aktosun. Reconstruction algorithms for interior and exterior spherical radon transform-based ultrasound imaging. *Proceedings of SPIE*, 7265:726511, 2009.
- [4] Yuan Xu, Lihong V. Wang, Gaik Ambartsoumian, and Peter Kuchment. Limited view thermoacoustic tomography. *Photoacoustic Imaging and Spectroscopy*, pages 61–73, 2009.

## 6 Appendices

Appendix A - Summary of mathematical modeling under UT Arlington subward

Appendix B - Reportable Outcome/Reference [3]

Appendix C - Reportable Outcome/Reference [4]

# Appendix A - Research related to Task 6 performed under UT Arlington subaward

17 September 2009

We consider a simple model of near-field ultrasound tomography, where a reflecting medium of interest is excited by spherical waves emitted from a transducer, and the backscattered echoes are registered by a receiver [11, 12]. Assuming an ideal propagative medium, where the speed of sound is constant, the signal registered at any given moment by the receiver is generated by reflections from all those points for which the sum of their distances to the emitter and the receiver is constant (depending on time and sound speed). In other words, those points are located on confocal ellipses with foci at the emitter and receiver locations, and the problem of image reconstruction in 2D boils down to the inversion of a transform integrating functions along such ellipses. In 3D one should consider a transform integrating along the family of surfaces of revolution (obtained by rotating the 2D ellipse around its main axis).

**Definition 1.** *The elliptical Radon transform (ERT) of  $f(x)$ ,  $x \in \mathbb{R}^2$  is defined as*

$$\tilde{R}f(p_e, p_r, r) = \int_{|x-p_e|+|x-p_r|=r} f(x) dl(x),$$

where  $dl(x)$  is the arc length of the ellipse  $|x - p_e| + |x - p_r| = r$ .

It is easy to see that the inversion of this transform is an overdetermined problem (recovering a function of 2 variables from a function of 5 variables). Hence, one should expect to be able to reconstruct  $f$  from restrictions of  $\tilde{R}f$  to 2-dimensional families of ellipses. From physical considerations we first restrict the locations of foci  $p_e$  and  $p_r$  (the acquisition geometry) to a curve  $S$

in  $\mathbb{R}^2$  (denoting the transform by  $\tilde{R}_S f(p_e, p_r, r) = \tilde{R}f(p_e, p_r, r)|_{p_e, p_r \in S}$ ). We consider the lines and circles for  $S$  in this project. Notice, that  $\tilde{R}_S f(p_e, p_r, r)$  is a three-parameter family, while  $f(x)$  is a function of two variables. There are several ways to reduce the dimension of the family of  $\tilde{R}_S f(p_e, p_r, r)$ . Motivated by tomographic models (e.g. [16, 3, 11, 12]) we will assume, that the distance between the emitter and the receiver stays constant. By matching the dimensions this way we further denote the ERT by  $\tilde{R}_S f(p, r)$ , where  $S$  is either a circle or a line, and  $p$  is the midpoint of the interval joining the foci of the ellipse.

Notice, that in the degenerate case when the emitter coincides with the receiver the ellipses become spheres and the ERT becomes a spherical (or circular) Radon transform (SRT). The latter has been extensively studied in the past for various applications of imaging and applied mathematics (e.g. [1, 2, 4, 8, 9, 10, 13, 15] and the references therein). In case of SRT various exact inversion formulae have been discovered for a limited number of acquisition geometries. These results can be divided into two categories: closed backprojection type inversion formulae, and expansions into series (usually involving some special functions). One of the goals of our project has been obtaining extensions of these results to the case of ERT, and the discovery of some new inversion algorithms. While the work in this direction is continuing, we can report certain progress here.

We developed an inversion algorithm using the algebraic reconstruction techniques based on the Kaczmarz method, which can work in any acquisition geometry. It also provides an effective mechanism for incorporation of certain side constraints to the reconstruction process, which is an extremely important tool for stabilizing the inversion in limited data problems. The developed algorithms have been numerically implemented in Matlab, and are currently being tested with both synthetic and experimental data. Two publications describing the developed methods and the obtained results are in preparation. The mathematical description of the inversion instabilities in limited data problems has been covered in [17].

We have also made certain progress in generalizing the inversion formulas for SRT using series expansion to the case of ERT. Most of the inversion formulas using series expansions for SRT are based on the fact, that this transform is either shift-invariant, or can become shift-invariant after a smooth change of variables. For example, the result of [13] is derived as follows. Let  $R_S$  be the 2D spherical Radon transform on the plane that integrates functions compactly supported inside the unit disk  $D$  over all circles

$|x - p| = \rho$  with centers  $p$  located on the unit circle  $S$ . Since this transform commutes with rotations about the origin, the Fourier series expansion with respect to the polar angle partially diagonalizes the operator, and thus the  $n$ -th Fourier coefficient  $g_n(\rho)$  of  $g = R_S f$  will depend on the  $n$ -th coefficient  $f_n$  of the original  $f$  only. Hence, the problem of reconstructing  $f$  from  $g$ , can be reformulated as a problem of reconstructing  $f_n$  from  $g_n$ . The latter requires solving an integral equation, which in [13] is done using the Hankel transform. In [14] the SRT is inverted in the case of a linear aperture by utilizing the shift invariance of the transform in the direction of the data acquisition line, and obtaining shift invariance in the orthogonal direction by a smooth change of variable. Then application of the 2-dimensional Fourier transform diagonalizes the operator, which enables the inversion. In case of a non-degenerate ERT in linear acquisition geometry, we have proved that there does not exist any smooth change of coordinates, which would make the transform shift-invariant in the second variable, hence one should not expect inversion procedures using Fourier techniques in this case. In the case of spherical acquisition geometry the elliptic transform  $\tilde{R}$  also commutes with rotations about the origin, hence the inversion method using the Fourier series expansion may allow generalization to ERT. We have reduced the problem of recovering  $f$  from  $g$  to the problem of recovering  $f_n$  from  $g_n$ . The latter is a non-trivial integral equation, and we currently work on its solution.

## References

- [1] M. L. Agranovsky, and E. T. Quinto, “Injectivity sets for the Radon transform over circles and complete systems of radial functions,” *J. Funct. Anal.*, **139** (1996), 383–413.
- [2] L.-E. Andersson, “On the determination of a function from spherical averages,” *SIAM J. Math. Anal.*, **19** (1988), no. 1, 214–232.
- [3] J. Coker, and A. Tewfik, “Multistatic SAR image reconstruction based on an elliptical-geometry Radon transform,” *2007 International Waveform Diversity and Design Conference*, 204–208, IEEE Conference Proceedings, 2007.
- [4] A. Denisjuk, “Integral geometry on the family of semi-spheres,” *Fract. Calc. Appl. Anal.*, **2** (1999), no. 1, 31–46.
- [5] L. Ehrenpreis, *The Universality of the Radon Transform*, Oxford Univ. Press 2003.
- [6] J. A. Fawcett, “Inversion of  $n$ -dimensional spherical averages”, *SIAM J. Appl. Math.*, **45** (1985), no. 2, 336–341.
- [7] D. Finch, M. Haltmeier, and Rakesh, “Inversion of spherical means and the wave equation in even dimension,”, *SIAM J. Appl. Math.*, **68** (2007), no.3, 392–412.
- [8] D. Finch, Rakesh, and S. K. Patch, “Determining a function from its mean values over a family of spheres,” *SIAM J. Math. Anal.*, **35** (2004), no. 5, 1213–1240.
- [9] I. Gelfand, S. Gindikin, and M. Graev, *Selected Topics in Integral Geometry*, Transl. Math. Monogr. v. 220, Amer. Math. Soc., Providence RI, 2003.
- [10] F. John, *Plane Waves and Spherical Means, Applied to Partial Differential Equations*, Interscience Publishers, 1955.
- [11] S. Mensah, and E. Franceschini, “Near-field ultrasound tomography,” *J. Acoust. Soc. Am.*, **121** (3), March 2007, 1423–1433.

- [12] S. Mensah, E. Franceschini, and M.-C. Pauzin, “Ultrasound mammography,” *Nuclear Instruments and Methods in Physics Research, Section A*, **571** (2007), no. 3, 52–55.
- [13] S. J. Norton, “Reconstruction of a two-dimensional reflecting medium over a circular domain: Exact Solution,” *J. Acoust. Soc. Am.*, **67** (1980), no. 4, 1266–1273.
- [14] S. J. Norton, “Reconstruction of a reflectivity field from line integrals over circular paths,” *J. Acoust. Soc. Am.*, **67** (1980), no. 3, 853–863.
- [15] S. J. Norton, and M. Linzer, “Ultrasonic reflectivity imaging in three dimensions: exact inverse scattering solutions for plane, cylindrical, and spherical apertures,” *IEEE Trans. Biomed. Eng.*, **28** (1981), 202–220.
- [16] D. Trad, T. Ulrych, and M. Sacchi, “Accurate interpolation with high-resolution time-variant Radon transforms,” *Geophysics*, **67** (2002), no.2, 644–656.
- [17] Y. Xu, L.-H. Wang, G. Ambartsoumian, and P. Kuchment, “Limited view thermoacoustic tomography,” in *Photoacoustic imaging and spectroscopy*, ed. L.-H. Wang, CRC Press, 2009.

# Reconstruction algorithms for interior and exterior spherical Radon transform-based ultrasound imaging

Ravi Shankar Vaidyanathan<sup>\*a</sup>, Matthew A. Lewis<sup>\*a</sup>, Gaik Ambartsoumian<sup>b</sup>, Tuncay Aktosun<sup>b</sup>

<sup>a</sup>Graduate Program in Biomedical Engineering, UTSouthwestern Medical Center at Dallas;

<sup>b</sup>Dept. of Mathematics, UT Arlington

## ABSTRACT

This work is concerned with the numerical implementation of a reconstruction algorithm developed to recover a function from its spherical means over spheres centered on a circle. The algorithm is experimentally verified by simulations using numerical phantoms. In the scheme of tomography, acoustic waves are generated by illuminating an object with a short burst of radio-frequency waves. In applications, like breast cancer imaging, which use modalities like photo-acoustic tomography (PAT) that model the acoustic pressures as spherical means, data are measured on the detectors located in a circle surrounding the object. This is then used to reconstruct the absorption density inside the object. In contrast, applications like bore hole tomography and improved Intravascular Ultra Sound (IVUS) imaging for prostate cancer, which use modalities like Radial Reflection Diffraction Tomography (RRDT), a ring of detectors placed exterior to the object, collect the acoustic waves as back-scattered field. This work uses a single algorithm to reconstruct functions from data collected using these two different techniques – one, by placing the object inside the ring of detectors, and the other, by placing the object exterior to the ring of detectors. The algorithm then draws a comparison between the two reconstructions. The case of bistatic ultrasound imaging, where the elliptical Radon transform is appropriate, is also discussed.

**Keywords:** Ultrasound Tomography, Spherical Radon, Elliptical Radon, Diffraction Tomography

## 1. INTRODUCTION

In imaging techniques like photo-acoustic tomography biological tissues [1] are irradiated with short pulse waves of energy, and ultrasound waves are subsequently generated. In medical modalities such as breast imaging [2] these waves are measured by sensors on the exterior surface of the tissues. Under the approximation that the speed of sound,  $c$ , is constant throughout the body, in a *monostatic* setup (where a single transducer acts as both the source and detector), the measured ultrasound waves are modeled as circular means of their reflectivity obtained over concentric circles centered at the measured point (fig 1). Formulas of the filtered back-projection to reconstruct the object were established [3] for a function supported in the ball in even dimensions. In this paper, we consider implementing this algorithm to reconstruct phantoms with no noise.

The algorithm is also implemented to synthetic data obtained by placing the ring of detectors exterior to the object. In applications like Radial Reflection Diffraction Tomography (RRDT) [4] that can be used in medical modalities such as prostate imaging , the object is external to transducer geometry (fig 2) and the transducers launch a primary field and collect the ultrasound waves as backscattered field. In such *multimonostatic* assemblies (where a single transducer acts both as a source and detector at multiple locations) the reconstruction techniques involve different kind of wave modeling. We implement the formula obtained in [3] to reconstruct object for this type of modality. With a different method, the result appears to be similar to reconstructions in the diffraction tomography technique [4].

The effect of the algorithm in reconstructing partial data is also analyzed. Reconstruction from incomplete data when the detectors are placed along a semi-circle surrounding the object leads to interesting observations which is analytically accounted for in [5].

Finally, we naively implement the same algorithm by slightly changing the filter to reconstruct data obtained in a *bistatic* setup (one transducer acts as a source and another acts as the detector). This method uses elliptical Radon transform to

model the data. There is no filtered back-projection kind of algorithm found in literature that reconstructs elliptical Radon transformed data.

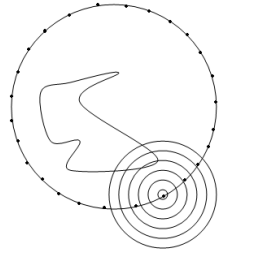


Fig.1 Object placed inside  
the ring of detectors

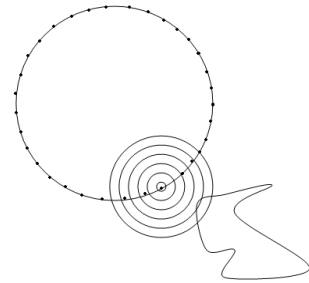


Fig.2. Object placed outside  
the ring of detectors

## 2. GEOMETRICAL SETUP

In near-field ultrasound tomography, where the waves are spherical and the sensors are point sources/receivers, various tomographic geometries are possible. Here, we discuss three possible 2-D geometrical setups in the case where the transducers are placed along a circle. An equivalent would be a transmitter/receiver being rotated about a fixed center like shown in fig 3.a. At each point on the circle the transducer emits a wave and receives the scattered wave back, an operation called as “pitch/catch” in the monostatic case [4]. In the 2-D case, the object to be reconstructed is in the plane perpendicular to the axis of rotation of the transducer. In Radial Reflection Diffraction Tomography (RRDT) algorithm, the data are collected as backscattered waves at various angular locations and the inversion is performed based upon a linear scattering model [6].

In this paper we implement an algorithm which inverts data obtained at various angular locations on a circle as projections which are spherical means (circle in 2-D with the transducer location as the center) of the function (object) to be reconstructed.

### 2.1 Monostatic setup

As discussed above, in the monostatic setup (fig. 4.a), the same transducer acts as both the transmitter and receiver. Assuming the speed of sound,  $c$ , constant inside the object, we can say that the time,  $t$ , for the pulse to reach the medium and time the echo takes to reach the receiver are equal. The loci of all points in the medium which satisfy the aforementioned condition will lie on a circle with ‘radius’  $t$ . Therefore if the resultant echoes are recorded as function of time, we will obtain a family of line integrals of the function along concentric circles centered at the source at a particular angle. We obtain such circular integrals at multiple angular locations along a circle. Our aim is to reconstruct the function from these projections.

From the setup explained above, we can parameterize a spherical Radon transform with two parameters, angle  $\theta$  and radius  $r$ . A symbolic statement of the forward equation would be the following:

$$G(\rho, \phi) = \int_{|\mathbf{R}-\mathbf{r}|} f(r, \theta) ds$$

where  $G(\rho, \phi)$  is the line integral of  $f(r, \theta)$  along the circle of radius  $\rho$ , whose center (the source transducer) lies on the circumference of the enclosing circle at angle  $\phi$ .

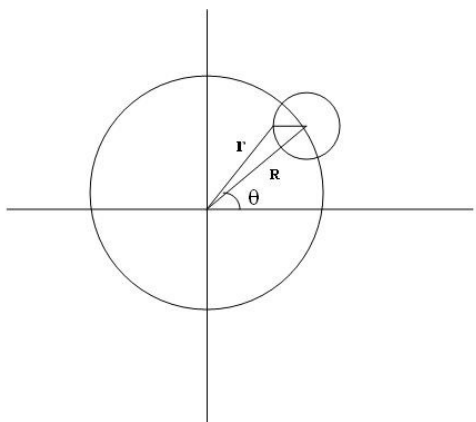


Fig.3. The circular integral of the function is obtained over a circle centered at the source transducer. $r$  is the distance from the origin to the scatterer and  $R$  is the radius of the circle along which the transducer rotates.

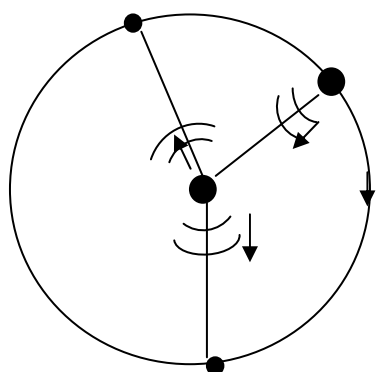
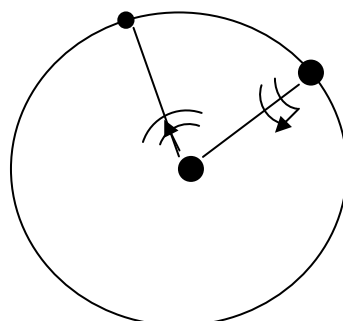
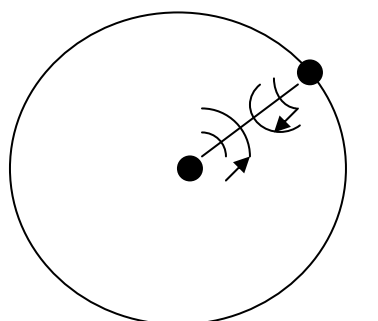


Fig.4. Various geometrical setups for a 2-D ultrasound tomography system where the transducers are placed along a circle –a. Monostatic – a single transducer acts both as transmitter and receiver. b. Bistatic – One transducer acts as a transmitter and other acts as receiver. c. Multistatic – One transducer transmits ultrasonic waves and many transducers act as receivers

## 2.2 Bistatic setup

As shown in fig. 4.b, in a bistatic setup, a pair of transducers moves along the circle. One transducer acts as a transmitter and the other acts as the receiver. If we consider the time from the emitter to the scatterer is  $t_1$  and from the scatterer to the receiver,  $t_2$ , and assume  $t_1+t_2$  is a constant, then the loci of all scatterers which satisfy this condition will lie on an ellipse. In this case the recorded resultant echoes at the receiver as a function of time will be line integrals of the function to be recovered over a family of ellipses.

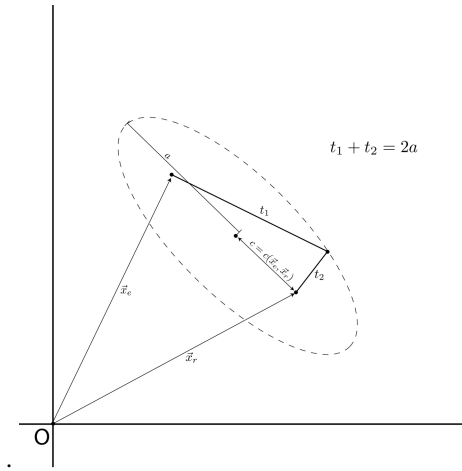


Fig.5. The line integral of  $f$  in the case of bistatic setup is obtained over an elliptical path. An ellipse is defined by five parameters.

There is no filtered backprojection (FBP) kind of algorithm in literature to invert an elliptical Radon transformed data. A Fourier transform based reconstruction is attempted in [7]. However, we implement the same filter suggested in [3] with a slight modification to invert elliptical Radon transformed data in a FBP fashion for a bistatic model.

To remark on the parameterization of the ellipse, there are five degrees of freedom. But to make the model practical and physical we can have constraints on two of the parameters and reduce the degrees of freedom to three. The problem still remains overdetermined.

## 2.3 Multistatic setup

Multistatic setup, as shown in fig.4.c, has one source and more than one receiver and this setup is rotated along a circle. Again a wave based tomographic image reconstruction is attempted in [4].

## 3. FILTERED BACKPROJECTION ALGORITHM

The problem of reconstructing the function from the circular integrals is similar to the classical problem of reconstructing the function from the projections in x-ray tomography. In fact, the circular Radon reconstruction reduces to classical Radon solution in the limit as the radius of the as the radius of the enclosing circle approaches infinity.

We were primarily inspired by the FBP algorithm suggested in [3] for inverting spherical Radon transformed data. The paper suggests an FBP algorithm with linear interpolation in two dimensions. The logarithmic filter suggested was dependent on the radial samples of the acquired data.

The algorithm was implemented in Matlab and for all  $(N+1)^2$  reconstruction points,  $N_\phi+1$  centers on S were summed up. If there are  $N^2$  pixels and if N is approximately equal to both the radial and angular samples, the algorithm requires  $O(N^3)$  operations.

## 4. METHODS AND RESULTS

### 4.1 Case 1: The object being placed inside the ring of detectors

The filtered-backprojection algorithm suggested in [3] was applied to 2-D synthetic data obtained from performing forward spherical Radon transform on a 100 by 100 Shepp-Logan phantom. In the first case, where the forward Radon was performed with the object inside the ring of detectors with a number of radial samples  $N_r=100$  and number of angular samples  $N_\phi=100$ . The sinogram obtained is depicted in figure 6b and the reconstructed image is shown in 6a.

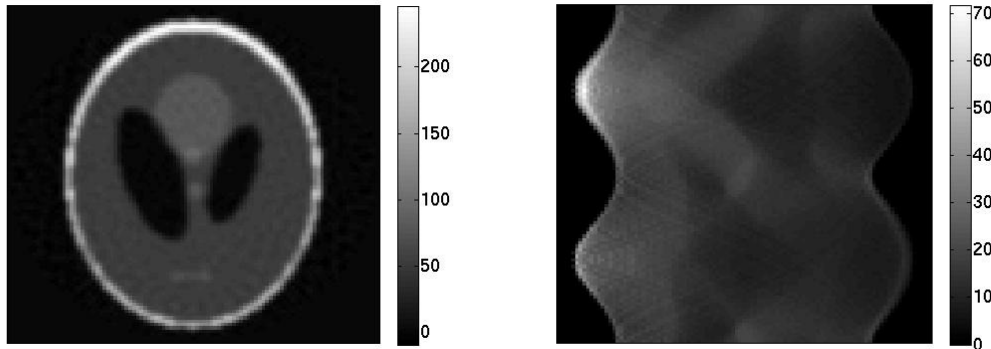


Fig.6a. Reconstructed image when the object is placed inside ring of detectors

Fig.6b. Corresponding sinogram

### 4.2 Case 2: The object being placed outside the ring of detectors

The same algorithm was applied to the object when it was placed outside the ring of detectors with the same  $N_r$  and  $N_\phi$ . The sinogram obtained is depicted in figure 7b and the reconstructed image is shown in 7a.

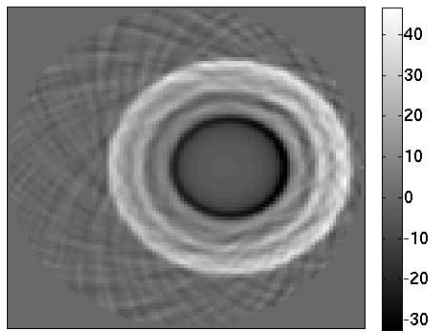


Fig.7a. Reconstructed image when the object is placed outside ring of detectors

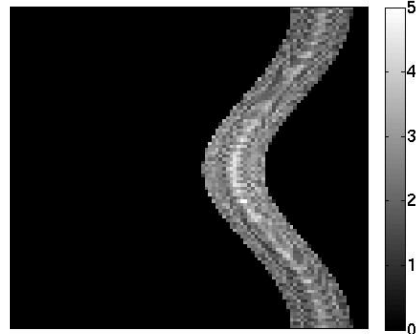


Fig.7b. Corresponding sinogram

#### 4.3 Case 3: Effect of incomplete data

We tried reconstructing the object by placing the transducers along a semi-circular arc at the bottom of the object. We used a different phantom to understand the effect of algorithm on incomplete data. The phantom is depicted in fig 8.a with the detector locations shown.

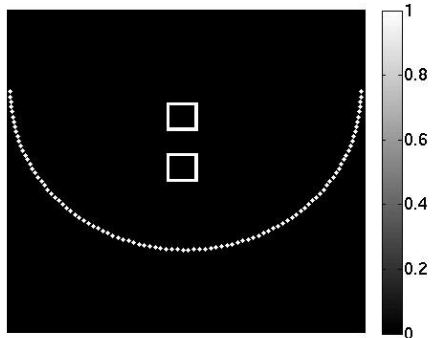


Fig.8.a. Phantom used for reconstruction from partial data. The detectors are placed along a semicircular arc at the bottom of the phantom.

The following images depict the sinogram and the reconstructed object:

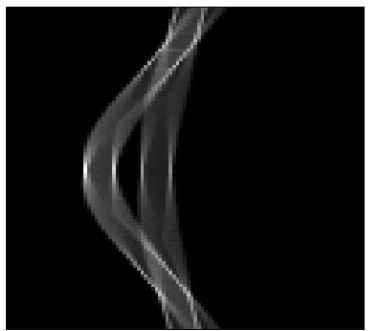


Fig. 8.b Sinogram obtained for incomplete data

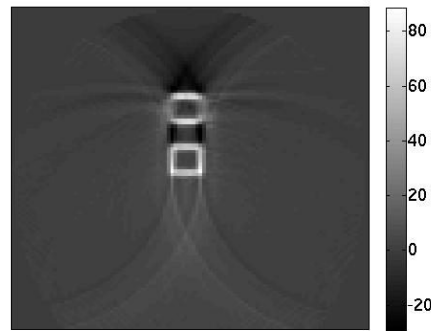


Fig. 8.b Reconstructed image

#### 4.4 Case 4: Applying a modified filter to reconstruct elliptical Radon transformed data

We finally implement the same algorithm with a slightly modified filter to reconstruct elliptical Radon transformed data. As explained in section 2.2, an ellipse has five degrees of freedom. We keep the distance between the foci constant (transmitter and receiver) and make it twice the dimension of the Shepp-Logan phantom we used previously. We also make the center of the foci lie on a circle. We also have an additional constraint on the rotation of the axis of the line connecting the foci. We keep this axis perpendicular to the radius of the enclosing circle.

The filter was modified by replacing the radial factor by minor axis of the ellipse. Projections contained samples of minor axes at every angular location. We used the Shepp-Logan phantom used previously. Fig 9.a shows the sinogram obtained and 9.b shows the reconstructed image.

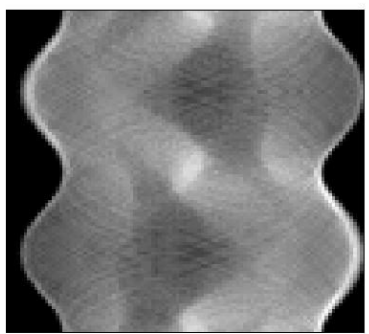


Fig. 9.a. Sinogram of the elliptical Radon transformed data

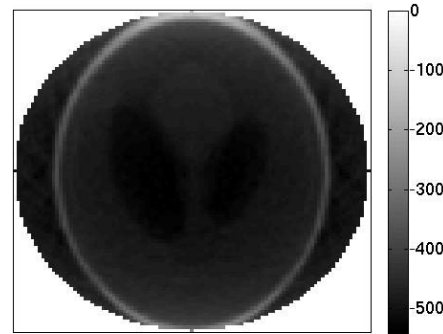


Fig. 9.b The reconstructed image with the modified filter

## 5. CONCLUSIONS

To conclude, we set out to implement the same reconstruction algorithm for the same mode of data acquisition with different modeling techniques. In the scheme of photo-acoustic tomography, as is the first case described above, the reconstruction works very well, whereas, in the model where the object is placed outside the ring of detectors, the algorithm seems to reconstruct only the artifacts.

With incomplete data, where the transducers are placed in a semicircular arc around the object, the reconstruction show similar results as explained in [5]. We observe the boundaries disappear in the case of incomplete data. Reconstruction from elliptical Radon transform data gives a low intensity image with a modified filter.

There is no existing FBP kind of algorithm for elliptical Radon transformed data. That can be considered for a future research work. The problem of exterior reconstruction can also be addressed as they have potential impact in medical imaging of breast and prostate cancer.

## 6. REFERENCES

- [1] Kostli K.P., Frauchiger D., Niederhauser J.J., Paltauf G., Weber H.P. and Frenz M., “*Optoacoustic imaging using a three-dimensional reconstruction algorithm*”, IEEE J. Sel. Top. Quantum Electronics, 7, 918-923, (2001).
- [2] Oraevsky A.A., Andreev V.A., Karabutov A.A., Fleming D.R., Singh G.Z.H. and Esenaliev R.O., “*Laser opto-acoustic imaging of the breast: detection of cancer angiogenesis*”. Bellingham, WA: SPIE, 3597, 352-363, (1999).
- [3] Finch D., Haltmeier M. and Rakesh, “*Inversion of spherical means and the wave equation in even dimensions*”, SIAM J. Appl. Math., 68(2), 392-412, (2007).
- [4] Lehman S.K. and Norton S.J., “*Radial reflection diffraction tomography*”, J. Acou. Soc. Amer., 116, 2158-2172, (2004).
- [5] Kutchment P. and Kunyansky L., “*Mathematics of thermoacoustic tomography*”, Euro. J. Applied Mathematics, 19, 191-224, (2008),
- [6] Devaney A.J., “*A filtered backprojection algorithm for diffraction tomography*”, Ultrason. Imaging, 4(4), 336-350, (1982).
- [7] Mensah S. and Franceschini E., “*Near-field ultrasound tomography*”, J. Acoust. Soc. Am, 121(3), 1423-1433 (2007).

\*ravi.vaidyanathan@utsouthwestern.edu; \*matthew.lewis@utsouthwestern.edu; phone 1 214-648-3659



# RECONSTRUCTION ALGORITHMS FOR INTERIOR AND EXTERIOR SPHERICAL RADON TRANSFORM-BASED ULTRASOUND IMAGING

Ravi Shankar Vaidyanathan, Matthew A. Lewis, Advanced Radiological Sciences  
UT Southwestern Medical Center at Dallas

Gaik Ambartsoumian, Tuncay Aktosun, Department of Mathematics  
The University of Texas at Arlington

UT SOUTHWESTERN  
MEDICAL CENTER

## Abstract

Photo- and thermo-acoustic tomography are non-ionizing imaging techniques that reconstruct internal photo (thermo) -acoustic source distributions from data acquired as projections by ultrasound detectors placed over a surface that encloses the object under study. They combine the high contrast in electromagnetic (EM) absorption between healthy and cancerous tissue with the high resolution of ultrasound. This mode of tomographic imaging has recently provoked an interest in researchers working on theoretical aspects of image reconstruction. Diffraction tomography methods for the same geometry exist and use the Born approximation for the reconstruction techniques.

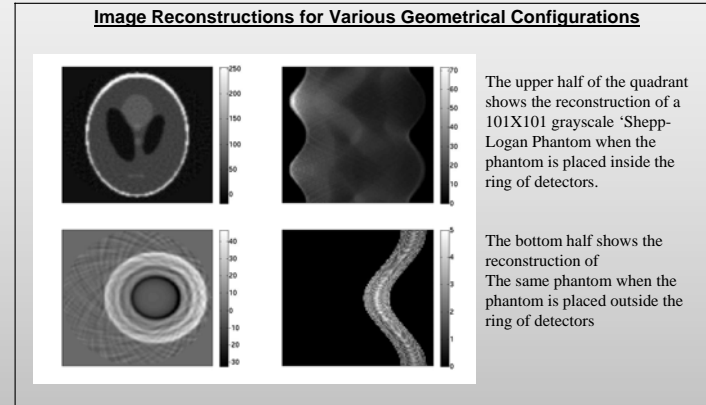
We investigate a Spherical Radon transform-based algorithm developed to recover a function from its spherical means over spheres centered on a circle. The algorithm is numerically implemented and experimentally verified using numerical phantoms. We implement the same algorithm to reconstruct data from projections obtained by placing the object inside the ring of detectors and placing it exterior to it. Both these arrangements are significant as they represent imaging techniques like Photo-Acoustic tomography and Radial Reflection Diffraction Tomography for endo-rectal prostate imaging.

## Rationale

Anticipating the introduction of clinical breast acoustic tomography systems where attempts are being made to solve the complete non-linear inverse scattering problem, we are considering a mathematical model that expresses data acquired as spherical Radon transformed projections. The idea behind this monostatic modality (the same sensor is used as both transmitter and receiver) is to illuminate an object by a short burst of radiofrequency waves which cause thermal expansion and subsequently generates an acoustic wave. The existing algorithms in both photo-acoustic and diffraction tomography successfully reconstruct the object if the acoustic waves are measured on the periphery or in the exterior of the object. Does the same algorithm work if the ring of detectors is placed exterior to the object? This is of interest because some anatomical constraints like in the case of prostate imaging require us to use an "exterior" geometry.

For further information:

Ravi.Vaidyanathan@UTSouthwestern.edu  
This work is supported by the U.S. Army Medical Research and Materiel Command under W81XWH-07-1-0640  
(PIs: MA Lewis & T Aktosun)



## Background

### Acoustic imaging geometry

Complex amplitude data for each receiver  $R_j$  and transmitter  $T_i$  is organized in multistatic response matrix  $K_{ij}$ .

- Far field – plane wave insonification, asymptotic scattering
- Near field – spherical waves, point sensors
- Monostatic – each sensor used as transmitter/receiver
- Bistatic – separate transmitter/receiver pairs
- Multistatic – many receivers per transmitter

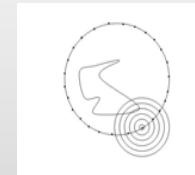
### Discrete FBP Algorithm

We are inspired by the derivation of a discrete *filtered back-projection* (FBP) algorithm (Finch, Haltmeier, Rakesh, SIAM J. Appl. Math. 68(2007) no.2, 392-412). We changed the 'radial' factor in the filter in the original FBP algorithm to use the minor axis of the ellipse rather than the radius of the projection.

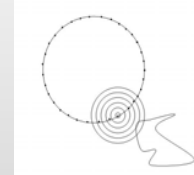
A discrete FBP for bistatic modeling involving elliptical radon transform which is of interest to tomographic imaging is not yet found in the literature.

The upper half of the quadrant shows the reconstruction of a 101X101 grayscale 'Shepp-Logan Phantom' when the phantom is placed inside the ring of detectors.

The bottom half shows the reconstruction of the same phantom when the phantom is placed outside the ring of detectors



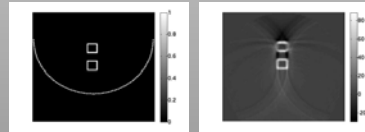
The algorithm proposed by Finch et al., shows good reconstruction results when the object is placed inside the ring of detectors



The algorithm seems to reconstruct only the artifacts when the object is placed outside the ring of detectors

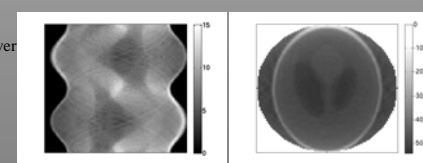
## Effect of Incomplete data

We tried reconstructing the object by placing the transducers along a semi-circular arc at the bottom of the object. We used a different phantom to understand the effect of algorithm on incomplete data. The phantom and the reconstructed image are depicted in figures below with the detector locations shown.



## Potential Impact

Ultrasound is not currently used for screening of breasts for non-palpable lesions; but with proven sensitivity and specificity, a non-ionizing ultrasonic method has the potential to allow earlier and more frequent breast screenings in at-risk patients. If breast compression can be avoided by the imaging technique, then ultrasound also represents a less stressful procedure for the patient. Breast ultrasound may be the only available technique for screening in the radiologically dense breasts of women under 40. Advances in early detection have already increased survivability, and there is reason to believe that improvements in breast screening with microcalcification-sensitive ultrasonic imaging will continue this trend.



In a bistatic setup the acquired data are modeled as elliptical Radon transform projections. If we assume the total time taken by the pulse to reach the scatterer and the echo to reach the receiver a constant, then the loci of all the scatterers which satisfy this condition will be an ellipse. We changed the 'radial' factor in the filter in the original FBP algorithm to use the minor axis of the ellipse rather than the radius of the projection.

There are no existing mathematical model in ultrasound tomography to image exterior objects which will be helpful in imaging diseases like prostate cancer.

---

# 6 Limited View Thermoacoustic Tomography

*Yuan Xu*  
Ryerson University

*Lihong V. Wang*  
Washington University in St. Louis

*Gaik Ambartsoumian*  
University of Texas at Arlington

*Peter Kuchment*  
Texas A&M University

## CONTENTS

6.1	Introduction .....	61
6.2	Mathematical Model and Reconstruction in TAT .....	62
6.2.1	Uniqueness of Reconstruction .....	63
6.2.2	Reconstruction Formulas and Algorithms.....	63
6.3	Limited View Problem .....	63
6.3.1	Uniqueness of Reconstruction from Limited View Data.....	63
6.3.2	Limited View Reconstructions .....	64
6.3.3	Wavefront Sets of Functions .....	64
6.3.4	“Visible” Singularities and Their Reconstruction .....	65
6.3.5	Half-Sphere Problem .....	66
6.3.6	Local Tomography and Singularity Sharpening.....	66
6.4	Numerical and Experimental Verification.....	67
6.4.1	Reconstruction from Synthetic Limited View Thermoacoustic Tomography Data .....	67
6.4.2	Reconstruction from Experimental Limited View Thermoacoustic Tomography Data .....	68
6.4.3	Discussion on Experimental Results.....	69
6.5	Additional Remarks and Conclusions .....	70
	Acknowledgments.....	71
	References.....	71

## 6.1 INTRODUCTION

Thermoacoustic tomography (TAT) employs the well-known [1–4] correlation between electromagnetic (EM) absorption of biological tissue and its physiological and pathological properties. To employ this contrast mechanism, a biological object is irradiated by a brief EM pulse, and the resulting thermoacoustic signals from the tissue are collected by ultrasound transducers to map the distribution of the radiation absorption within the sample (e.g., Refs. [5–9]). TAT thus combines the good spatial resolution of ultrasound imaging with the good contrast in EM absorption.

The problem we address in this chapter is of limited data (limited view), when transducers cannot be placed around the complete object. This situation is very common in TAT, for instance in its applications to breast imaging, where only a half sphere, rather than a sphere is available for placement. The question that arises is the theoretical and practical possibility of reconstruction from limited view data. Although, as we will see, mathematically rigorous uniqueness results exist that guarantee the theoretical possibility of reconstruction from limited view data, the practical situation is somewhat different. Namely, some features of the object

to be imaged (which we dub “invisible”) are practically impossible to reconstruct, because they suffer from a mandatory blurring. Any attempts to overcome this difficulty are futile, unless some prior information about the object or missing data is incorporated, or the very physical set up of the measurement is altered. On the contrary, the “visible” details are easy to reconstruct stably. It is thus important to understand these limitations due to limited data. Limited view problems have been studied extensively in other, more traditional, types of tomography, such as x-ray, SPECT, diffraction tomography, and reflectivity tomography (e.g., Refs. [10,11,13–18]). The TAT situation is similar and has been discussed in various ways in Refs. [19–27]. Although the underlying mathematical technique is rather involved, the final results are easy to understand and use. The goal of this chapter is to review these results and to provide the relevant references. We will not attempt to go through the rigorous mathematical technicalities, but rather explain the basic ideas. Correspondingly, the results will sometimes be stated, when the authors feel no danger of misuse, without some necessary technical conditions under which they are proven. References, however, will be given where the rigorous details can be found.

A significant limitation of what is described in this chapter is that the speed of ultrasound in the imaged tissue is assumed to be constant. The case of a variable speed could also be treated, but this would require a somewhat different and more complex consideration, which apparently has never been completely implemented.

The paper is structured as follows: In the next section, we state the model and briefly review the existing uniqueness results, reconstruction formulas, and procedures for the full data view problem. The section that follows contains the description of how the limits of view influence the uniqueness and reconstructions. It is explained how one can determine which interfaces in the object will be blurred in the reconstructed image due to the limited view. We also introduce in this section necessary simple mathematical notions. Then the next section presents numerical examples (both from synthetic and experimental data) that illustrate the concepts. All mathematical conclusions are equally applicable to photoacoustic tomography.

## 6.2 MATHEMATICAL MODEL AND RECONSTRUCTION IN TAT

The accepted mathematical model of TAT involves quite a few physical constants. As it happens, their presence is irrelevant for understanding the concepts and using the limited view results. We thus present here a simplified model, where all constants are assumed to be equal to one. The full-blown models with all the complications (which do not influence the issue we discuss here), as well as more details and references, can be found in surveys [28–30] and in chapters [31,32] in this volume.

With this simplification, the model of TAT is described by the following wave equation problem:

$$\begin{cases} p_{tt} = v_s^2(x) \Delta_x p, & t \geq 0, \quad x \in \mathbb{R}^3 \\ p(x,0) = f(x), \\ p_t(x,0) = 0, \\ p(y,t) = g(y,t) \text{ for } y \in S, \quad t \geq 0. \end{cases} \quad (6.1)$$

Here  $p(x,t)$  is the pressure at the point  $x$  and time  $t$ ,  $v_s(x)$  is the speed of the ultrasound propagation in the tissue,  $S$  is the observation surface where the transducers are placed,  $g(y,t)$  is the measured data, i.e., the value of the pressure at time  $t$  measured at the transducer’s location  $y \in S$ , and  $f(x)$  is the object to be reconstructed. As we have already mentioned, the results described here apply to the case of a constant sound speed only. We can also assume that  $v_s = 1$ , thus arriving at the simpler equations

$$\begin{cases} p_{tt} = \Delta_x p, & t \geq 0, \quad x \in \mathbb{R}^3 \\ p(x,0) = f(x), \\ p_t(x,0) = 0, \\ p(y,t) = g(y,t) \text{ for } y \in S, \quad t \geq 0. \end{cases} \quad (6.2)$$

In this (constant speed) case, the well-known Kirchhoff–Poisson formulas (see, e.g., Refs. [33,34]) allow one to represent the solution  $p(x,t)$  in terms of the spherical means of the function  $f(x)$

$$(Rf)(y,t) := \frac{1}{4\pi} \int_{|\omega|=1} f(y+t\omega) d\omega \quad \text{for } y \in S. \quad (6.3)$$

Thus, knowledge of the data  $g(y,t)$  is equivalent to knowing the integrals of the unknown function  $f$  over all spheres centered at transducers’ locations  $y \in S$ . One immediately notices a similarity with the standard Radon transforms for x-ray tomography or MRI, where the integration is done over lines or planes rather than spheres. And indeed, most of the standard tomographic results and techniques find their analogs in TAT, albeit many aspects become much more involved (see, e.g., Refs. [28–32,35–43]). We now address the uniqueness of reconstruction and reconstruction procedures in TAT.

The reader can notice that in all feasible applications, function  $f(x)$  to be reconstructed does not have “infinite tails”, i.e., vanishes outside of a bounded domain. Moreover, in most practical applications, it is true that its support is completely surrounded by the observation surface  $S$ . In what follows, this will be assumed (some results and inversion formulas might fail unless this is satisfied [30,31]).

We first assume the knowledge of the full data  $g(y,t)$  for an observation surface  $S$ , which is a sphere surrounding the support of the image  $f(x)$ . The case of limited-angle data will be considered in the next section.

A similar problem to the one we have just described in 3D can also be considered in other dimensions. For TAT, only dimensions 2 and 3 are relevant (the need to use a 2D problem arises, for instance, when one uses linear, rather than point-like, detectors [24,25]).

### 6.2.1 UNIQUENESS OF RECONSTRUCTION

The first question to answer is whether the data determines function  $f$  uniquely, i.e., which observation surfaces  $S$  provide uniqueness of reconstruction. In 2D, this was resolved in Ref. [35]. There is still no complete solution in 3D (see Refs. [15,28–32,35,38–41] for surveys and references). However, from the practical point of view, there is no problem. Indeed, it has been known at least since Ref. [44] (see also the references just mentioned and Ref. [45]) that if the surface  $S$  is closed, e.g., a sphere, and if  $f$  has a bounded support (not necessarily surrounded by  $S$ ), then there is uniqueness.\* When  $S$  is a cylinder, uniqueness also holds, and if  $S$  is a plane, uniqueness holds if  $f$  vanishes on one side of the plane (otherwise an odd function  $f$  with respect to the plane provides a counterexample). This essentially covers any feasible full-view TAT situation.

Now, when uniqueness is established, one wonders how to actually reconstruct the image  $f$ .

### 6.2.2 RECONSTRUCTION FORMULAS AND ALGORITHMS

Although the area had experienced a slow start, there has been a large variety of inversion formulas and algorithms developed lately (at least for the case of a constant sound speed that we consider here). One can find a thorough discussion of inversion formulas and reconstruction algorithms in the surveys [31,32] in this volume, as well as in Refs. [29–32]. We will just say a few general words about these, since the details of a particular algorithm do not seem to affect the general conclusion that we will make later about the limited view problems in TAT.

Explicit inversions based on Fourier transform techniques have been developed in the case of a planar observation surface  $S$  (see, e.g., Refs. [16,46–50]).

The most interesting case of a spherical surface  $S$  was first rigorously treated in Refs. [51,52], where the rotational invariance of the problem was used to expand the data and the image into Fourier series with respect to the angle. This resulted in explicitly solvable Abel-type integral equations for each Fourier coefficient (a la A. Cormack’s work on x-ray CT). While the 2D formulas of Ref. [51] involved numerical instabilities, this was fixed in the 3D reconstructions of Ref. [52].

For quite some time, there had been no explicit filtered backprojection-type formula obtained for any closed observation surface  $S$ , and even the possibility of such a formula was questioned. Finally, in Ref. [38], such formulas were found for all odd dimensions when  $S$  is a sphere, and then extended to even dimensions in Ref. [53]. A different 3D backprojection-type formula was obtained in Ref. [54]. A backprojection formula for arbitrary dimension was found in Ref. [55], which in 3D coincided with the one in Ref. [54]. It is interesting to note that the series of formulas in Refs. [38,53]

and in Refs. [54,55] are not equivalent on nonperfect data, albeit they seem to work numerically equally well [30,31]. A different derivation of formulas in Ref. [38] has recently been proposed [56]. No closed form analytic formulas are known for surfaces  $S$  that are not spheres, cylinders, or planes.

An interesting series expansion inversion procedure that theoretically works for any closed observation surface  $S$  was suggested in Ref. [57]. The expansion of the image  $f(x)$  into the eigenfunctions of the Laplace operator  $\Delta$  inside  $S$  with zero Dirichlet conditions on  $S$  is obtained in terms of the corresponding expansion of the measured data. It was shown in Ref. [57] that a cubic surface used as  $S$  rather than a sphere works much better, leading to very fast, accurate, and efficient reconstructions. This series expansion procedure was generalized to variable sound speeds in Ref. [43], albeit it is doubtful that this can lead to efficient computations.

Although having analytic inversion formulas always helps in tomography, it is also known that reconstructions can often be efficiently done without having explicit formulas, by either algebraic techniques, or their combination with analytic preconditioning. This is true in TAT as well. Namely, it is not hard to write a good approximate inversion operator (technically called a **parametrics**) that gives a sufficiently good approximate reconstruction and preserves the locations and strengths of all singularities of  $f$  (e.g., sharp boundaries). Then one can bootstrap the quality of reconstruction by a standard iterative numerical procedure (e.g., Refs. [23,58,59]).

Another option is the so-called time reversal. Here one solves the wave equation backward in time, starting with a sufficiently large time, when the signal essentially disappears. Then when time  $t=0$  is reached, the image  $f(x)$  is recovered (e.g., Refs. [36–38,43,60,61] and references therein).

Various other discussions of inversion procedures and relevant references can be found in Refs. [29–31,36,37,62–71].

## 6.3 LIMITED VIEW PROBLEM

We now switch to the situation of our main interest in this paper—limited view TAT. Suppose that  $S$  is a sphere (or some other closed surface) surrounding the image  $f$ , and the only possible locations of transducers belong to a 2D piece  $\Gamma$  of  $S$ . In this case, we only have the data  $g(y,t)$  collected at the locations  $y$  in  $\Gamma$ , rather than from the whole sphere. In this case, we face a limited angle (limited view) problem.

### 6.3.1 UNIQUENESS OF RECONSTRUCTION FROM LIMITED VIEW DATA

Let us first discuss the uniqueness of recovering the image from the data. The dimension count shows that one should use a two-dimensional piece  $\Gamma$  of  $S$  in order to expect uniqueness. Suppose that  $S$  is an analytic surface (say, a sphere) and  $\Gamma$  its two-dimensional piece. It follows from the results of Ref. [35] that if uniqueness of recovery from the data collected on the whole  $S$  is known, then there is also uniqueness of recovery with data collected on  $\Gamma$ . For instance, since the sphere is

\* For the uniqueness result to hold, it is not necessary to require that  $f$  vanishes at infinity, sufficiently fast decay at infinity also suffices [45]. However, in practical situations,  $f$  does vanish at large distances.

analytic and since for the whole sphere uniqueness of reconstruction is known (see the preceding section), we conclude that with the data on any full-dimensional piece  $\Gamma$  of the sphere, no matter how tiny, solution of the TAT problem is unique. The same holds for a 2D piece of any closed analytic surface.<sup>†</sup>

Although this says that the limited view data is theoretically sufficient, anyone trying to do reconstructions faces problems, mostly related to blurring of some parts of the image. This effect is no accident and can be predicted, as explained in the rest of the chapter. Let us look first at how one can try to reconstruct the image from limited view data.

### 6.3.2 LIMITED VIEW RECONSTRUCTIONS

The simplest thing one can try is just to replace the missing data with zero values<sup>‡</sup> (the procedure often called zero-filling or zero-padding) and then reconstruct the image as if the data were complete. In advance, one might not expect any reasonable outcome from this, however the following observations appear, independently of the exact procedure involved:

1. Some (we will call them “visible”<sup>§</sup>) parts of the tissue interfaces and other singularities contained in the true image are seen clearly and at the right locations. These parts do not depend upon the exact technique used, but do depend on the view angle available.
2. Other parts of interfaces blur away.
3. “Smooth” details of the object, i.e., exact values of  $f(x)$  get distorted, in some areas significantly.

In most cases in tomography, limited data problems allow no exact reconstruction formulas. In the rare cases when these do exist, this does not change the effects listed above. As we explain below, there is a good reason for this, and, in fact, the “invisible” and “visible” parts of singularities can be easily predicted by a simple geometric consideration. In order to do so, we need to introduce some technical notions from the so-called microlocal analysis first (see, e.g., Ref. [72] for simple introduction and Refs. [15,18,23,35,39,73,74] for applications in integral geometry and tomography).

### 6.3.3 WAVEFRONT SETS OF FUNCTIONS

Our goal is to apply known results of integral geometry concerning singularity reconstruction [11,12,15,39] to TAT [19,23]. The exact description of these would require some notions of microlocal analysis, in particular the notion of a wavefront set of a function [72]. In tomographic problems, in particular in TAT, one is most interested in only one type

of singularity: the jump of  $f(x)$  across an interface (a curve in 2D or a surface in 3D). So, we will describe the wavefront set in this case first. Let  $f(x)$  be smooth except for a jump across a smooth surface  $L$  (in 2D case,  $L$  is a curve), then the wavefront set  $WF(f)$  of  $f(x)$  consists of pairs  $(x, \xi)$ , where point  $x$  belongs to  $L$  and  $\xi \neq 0$  is a nonzero vector normal to  $L$  at  $x$ , as shown in Figure 6.1.

Before introducing the wavefront set in the general case, let us recall that smoothness is reflected as decay in the Fourier domain. Indeed, if  $f(x)$  is smooth and has compact support (or decays sufficiently fast with its derivatives), then its Fourier transform  $\hat{f}(\xi)$  decays faster than any power of  $|\xi|$  in all directions of the  $\xi$ -space. If we are interested in detecting the smoothness of  $f$  only locally, near a point  $x_0$ , we cut other parts off by multiplying  $f$  by a smooth function  $\phi$  that is non-zero only near  $x_0$ . Then, again, the Fourier transform  $\widehat{\phi f}(\xi)$  of the product decays faster than any power of  $|\xi|$  in all directions of the  $\xi$ -space. Well, what does it mean now that  $f$  is **not smooth** near  $x_0$ ? This means that  $\widehat{\phi f}(\xi)$  will not be decaying, unless  $\phi$  vanishes at  $x_0$ , which we will prohibit. However, it might still decay **in some directions**. This now leads to the general definition (e.g., Refs. [39,72]) of the wavefront set, which picks up for each point  $x_0$  the bad directions  $\xi_0$  only. It thus consists of pairs  $(x, \xi_0)$ , where  $\xi_0$  must be a nonzero vector (in order to determine a direction). It is easier to describe which pairs  $(x_0, \xi_0)$  (where  $\xi_0 \neq 0$ ) **do not** belong to the wavefront set  $WF(f)$  of a function  $f$ . Namely, this happens if there is a neighborhood  $u$  of  $x_0$  and a conic neighborhood

$$V_\epsilon = \left\{ \xi \neq 0, \text{ such that } \left| \frac{\xi}{|\xi|} - \frac{\xi_0}{|\xi_0|} \right| < \epsilon \right\}$$

of the direction  $\xi_0$ , such that for any smooth function  $\phi$  supported inside  $u$ , the Fourier transform  $\widehat{\phi f}(\xi)$  of the function  $\phi f$  decays to zero faster than any power of  $|\xi|$  when  $\xi \rightarrow \infty$  in  $V_\epsilon$ . The role of the function  $\phi$  is to eliminate the possible bad behavior of  $f$  away from  $x_0$  and keep only the local

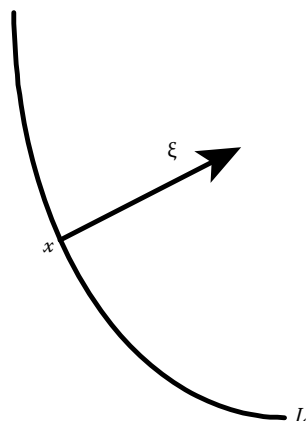


**FIGURE 6.1** If  $f(x)$  is smooth, except a jump singularity across  $L$ , then its wavefront set  $WF(f)$  consists of pairs  $(x, \xi)$ , where  $x$  belongs to the jump interface  $L$ , and  $\xi$  is a nonzero vector normal to  $L$  at  $x$ . (Reproduced from Xu, Y., L.V. Wang, G. Ambartsumian, and P. Kuchment, *Med. Phys.* 31(4):724–33, 2005. With permission.)

<sup>†</sup> A similar result holds also in x-ray CT, where limited view data uniquely determine the image. This immediately follows from the projection-slice theorem and analyticity of the Fourier transform of a compactly supported function.

<sup>‡</sup> It is advisable sometimes to smooth out the jump between zeros and actual data.

<sup>§</sup> Another name sometimes used is “audible” [39].

information about properties of  $f$  at  $x_0$ . Thus, the wavefront set of  $f$  carries the information about singularities of  $f$ , which is localized both in spatial variable  $x$  and frequency variable  $\xi$  (the word used is “microlocalization”, and thus “microlocal analysis”). Projecting the wavefront set onto the space component  $x$  (by forgetting the frequency variable  $\xi$ ), one obtains the so-called singular support of  $f$ , i.e., the set of all singularities of  $f$ —points near which  $f$  is not smooth. For instance, it is easy to check that the wavefront set of the delta function consists of  $(0, \xi)$  for any  $\xi \neq 0$ .

### 6.3.4 “VISIBLE” SINGULARITIES AND THEIR RECONSTRUCTION

The general idea of the microlocal approach to limited view problems is the following [11] (see a somewhat different, more limited approach in Ref. [12]). One tries to determine which wavefront set elements  $(x, \xi)$  of the object  $f$  lead to singularities, i.e., wavefront set elements in the measured data  $g$ . This can be done by the technique of the so-called Fourier integral operators (FIOs) [73,74], which is beyond the scope of the current consideration. If such a pair  $(x, \xi)$  does lead to a singularity in  $g$ , it is called “**visible**” or “**audible**”. Such wavefront set points of the object can be stably reconstructed from the data  $g$ , and thus the singularity will show up in the reconstruction. If a particular wavefront set point does not influence the singularities of the data  $g$  (i.e., it is smoothed out), it becomes “**invisible**” and thus will be blurred away. This blurring effect is intrinsic to the problem and cannot be overcome by changing analytic or numerical techniques, unless some extra information is incorporated into the problem.

This concept is not hard to understand. Imagine, for instance, that the operator that maps the unknown  $f$  into the data set  $g$ , turns all images even the ones with singularities, into smooth functions  $g$ . In the Fourier domain, this can be interpreted as an operation that turns slowly decaying Fourier transforms into the ones that decay faster than any power. For instance, one can imagine that this is done by applying a filter that decays extremely fast, and essentially acts as a low-pass filter. Trying to invert the procedure and reconstruct the object  $f$  from the data  $g$ , one runs into trouble, since the required filters will grow faster than any power (often exponentially). This clearly indicates impossibility of stable reconstruction of high-frequency components, and thus of any sharp details.<sup>¶</sup> A “microlocal” extension of this consideration shows that if some part of the wavefront set (i.e., a singularity) of the image  $f$  does not contribute to the wavefront set of the data, then this singularity cannot be stably recovered from the data.

It is thus important to be able to understand in advance which wavefront set elements  $(x, \xi)$  of the (unknown)  $f$  would lead to some wavefront set elements in  $g$ . This would determine which singularities are “visible” from the data  $g$ .

<sup>¶</sup> One faces such instabilities, for instance, trying to solve the heat equation back in time, or dealing with electrical impedance imaging or optical tomography.

Fortunately, there is a very simple answer to this question in the cases of x-ray tomography, SPECT, TAT, and some other imaging methods [11,15,18,19,39] (while its justification is very nontrivial). We will describe it following Ref. [19] (see also Ref. [23]), as applied to TAT:

#### The “visibility” condition

An element  $(x, \xi)$  of the wavefront set of  $f$  cannot be recovered looking at the singularities of the spherical integrals data, unless there is a detector location and a sphere centered at this location that passes through the point  $x$  and is normal to  $\xi$  at this point. In other words, in TAT one can see without blurring only those parts of the interfaces that can be touched tangentially by spheres centered at detector positions. This means that in order to recover stably (i.e., without blurring) the interface  $L$ , one needs to have for each point of  $L$  a detector located along the normal line to  $L$  at this point. If for some part of  $L$ , the normals do not pass through the detectors, this part will be “invisible” and will be mandatorily blurred away.

**Remark 1** *This principle does not depend upon a particular reconstruction method. So, a bad method can increase blurring, but even the best methods cannot recover sharply the “invisible” interfaces. This is why in this text we do not go into any details of reconstructions. Certainly, incorporation of additional a priori information about the image (e.g., that it consists of a few simple “blocks”) could potentially lead to improvements.*

The visibility condition described above is not hard to understand. Indeed, assume for simplicity that the integration that produces the measured data is done along planes rather than spheres, and that the interface is also planar. Then, if one integrates along a stack of parallel planes  $x \cdot \omega = s$  that is not parallel to the interface  $L$  (i.e., the normal vector  $\omega$  to the plane of integration is not normal to  $L$ ), the singularity of  $f$  along the interface is smoothed out, and the resulting value depends on  $s$  smoothly. Only if one has at one’s disposal a set of planes parallel to the interface (i.e.,  $\omega$  is normal to  $L$ ), then the integration of  $f$  will result in a singularity with respect to  $s$ . This indicates that invisible parts of the wavefront set do not show up as singularities in the measured data, and thus cannot be stably reconstructed. This hand-waving explanation can be made precise, with substantial technical effort.

Notice that if at some location  $x$ , any line passing through  $x$  crosses a detector position, then for any image, we expect its details near  $x$  to be reconstructed sharply. This leads us to the following notion:

**Definition 2** *Suppose that detectors can be located along a 2D (1D in the planar case) piece  $\Gamma$  of the observation surface  $S$  only. The **detectable region** consists of such points  $x$  inside  $S$  that every line passing through  $x$  crosses  $\Gamma$ .*

According to the visibility condition, any object supported inside the detectable region will be sharply reconstructed, while the objects reaching outside the detectable region will have some parts of their interfaces blurred away.

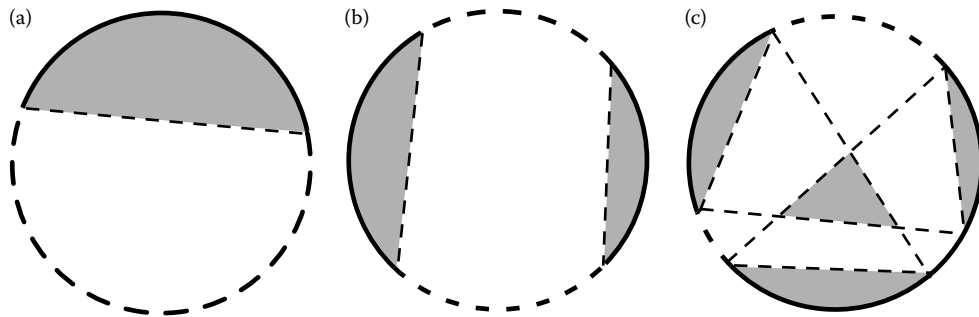


**FIGURE 6.2** (a) Illustration of the “detectable regions” (shaded areas) of circular Radon transformation, when the detector moves along a single arc (solid) of a circle. (b) Two arcs. (c) Three arcs. (Reproduced from Xu, Y., L.V. Wang, G. Ambartsoumian, and P. Kuchment, *Med. Phys.* 31(4):724–33, 2005. With permission.)

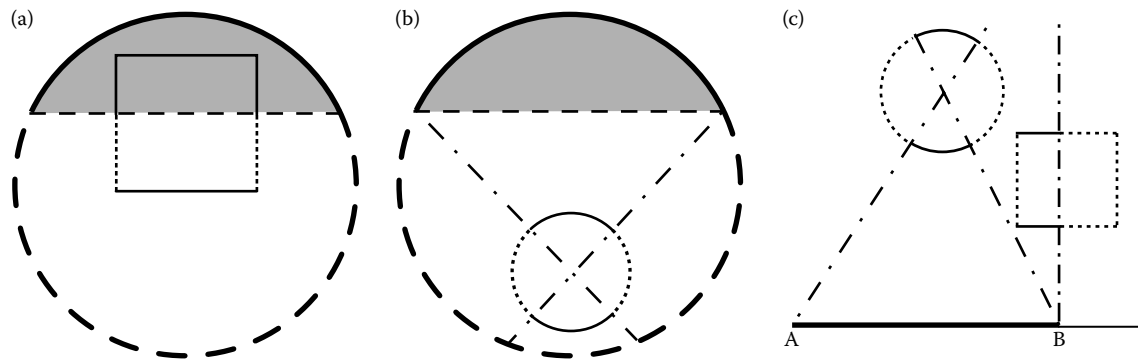


**FIGURE 6.3** (a) “Visible” (solid line) and “invisible” (dashed) boundaries of a square object, and the “detectable regions” (shaded areas) when the detector moves along an arc (solid). (b) Same as (a) for a disk phantom. (c) Same as (a) except that the detector moves along the line segment AB and the objects are a square and a disk. The “visible” boundaries are expected to be recoverable stably, while the “invisible” boundaries should be blurred away. (Reproduced from Xu, Y., L.V. Wang, G. Ambartsoumian, and P. Kuchment, *Med. Phys.* 31(4):724–33, 2005. With permission.)

Figure 6.2 illustrates the detectable regions. Figure 6.3 shows the expected behavior of the reconstructed interfaces of simple square and disk phantoms with limited view data.

Results of reconstructions from synthetic and experimental data, which confirm this conclusion, are shown in Section 6.4.

### 6.3.5 HALF-SPHERE PROBLEM

A particular case of interest, which has attracted the attention of several researchers, is when the detectors can be placed along half of the observation sphere  $S$ , and thus the detection region is the corresponding half-ball. It is assumed that the object is located inside the detection region. Then, the principle discussed in the previous section predicts that all singularities of the object are “visible” and thus reconstructions should be sharp. If one attempts to zero-fill the data from the other half sphere and use any of the standard reconstruction methods, the interfaces truly remain sharp, but the intensities deteriorate towards the missing equator. Having an exact reconstruction formula for half-sphere data would fix this problem, but such a formula has not been found so far.\* So, different partial remedies for this ailment have been sug-

gested: better approximate inverses, corrective coefficients, numerical minimization, using range conditions for recovering the missing data, etc. (e.g., Refs. [22,26,27]). A very recent work [77] shows great promise for the final resolution, albeit at the moment of writing this chapter, not all necessary details have been filled in.

### 6.3.6 LOCAL TOMOGRAPHY AND SINGULARITY SHARPENING

We would like to mention briefly the principle of the so-called **local tomography** [18,78–80]. In this method, before backprojection, an additional growing filter in the frequency domain is applied in order to sharpen singularities. The resulting reconstruction has incorrect numerical values of  $f(x)$ , but significantly emphasized interfaces and other singularities, which, for instance, can be useful when small blood vessels or region of interest tomography are of interest. Local tomography applies to TAT as well [19,23]. In the case of limited view data, it also recovers the “visible” parts of the interfaces only. Some of the reconstructions shown in the next section include their local tomography counterparts.

It is interesting to notice (see more about this in the following section), that transducers’ responses often act as that extra filter needed for local tomography, and thus boundaries are emphasized without any extra effort.

\* In SPECT, a similar problem waited quite a long time before its satisfactory resolution [75,76].

## 6.4 NUMERICAL AND EXPERIMENTAL VERIFICATION

In this section, we will illustrate our theoretical analysis and conclusions with reconstructions [23] from both synthetic and experimental (i.e., collected from a physical phantom) TAT data. We do not mention details of specific reconstruction methods used because, as explained earlier, the “visibility-invisibility” effect does not depend on the method used.

### 6.4.1 RECONSTRUCTION FROM SYNTHETIC LIMITED VIEW THERMOACOUSTIC TOMOGRAPHY DATA

A numerical phantom that contains four sharp and one soft inclusion is shown in Figure 6.4. Among the sharp inclusions, we have one large and two small squares and one disk. The object value is set to be 0.5 within the largest square, unity within other sharp inclusions, and zero elsewhere. Inside the “soft” circular inclusion, this value drops linearly with the radius from unity at the center to zero at the interface, in order to simulate a gradual interface. The imaged field of 154 mm by 154 mm is mapped with a  $128 \times 128$  mesh. The detection circle has a radius of 133 mm and is centered at the center of the picture. We scan 200 steps in all the simulations. The gray scale and the scale bar of the images are shown below the images in Figure 6.5. The top row of reconstructions employs the local tomography formula that emphasizes the boundaries. The next one uses the approximate filtered-backprojection (FBP) formula in Ref. [23], and the lowest one shows the improvements

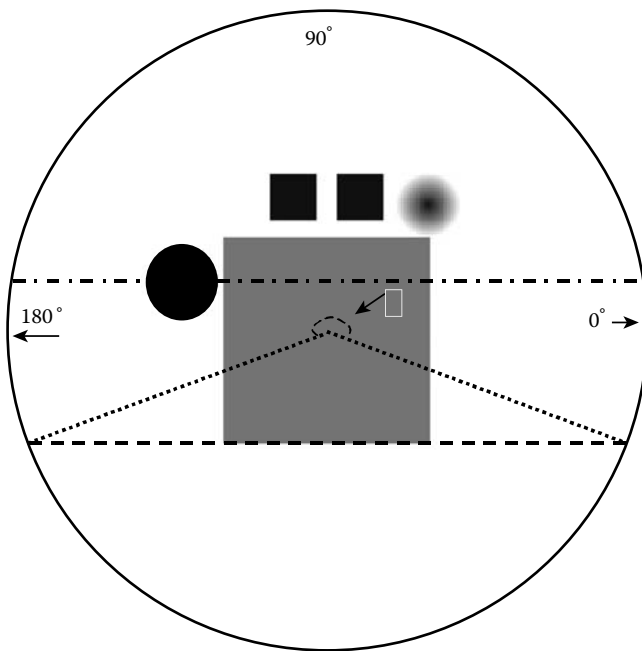


**FIGURE 6.4** Diagram of inclusions in TAT (used in Figure 6.5). The value of the image  $f(x)$  is set to be 0.5 in the largest square, and unity within other sharp inclusions, and zero elsewhere. Inside the “soft” circular inclusion, this value drops linearly with the radius from unity at the center to zero at the interface. (Reproduced from Xu, Y., L.V. Wang, G. Ambartsoumian, and P. Kuchment, *Med. Phys.* 31(4):724–33, 2005. With permission.)

achieved by running the algebraic reconstruction method (TCG), starting with the FBP as an initial guess [23].

The left column uses only the data collected from the  $\pi/2$  detection arc in the first quadrant. None of the phantom inclusions fit into the “detectable region”. One can see that all parts of the inclusion boundaries the normals to which do not intersect the detection arc are blurred (even in the local tomography reconstruction). Other parts of the boundaries are sharp. This is in perfect agreement with our theoretical prediction. The soft inclusion is not significantly affected by the artifacts.

The middle column employs the data collected from the detection arc of approximately 217 degrees (the angle  $\theta$  in Figure 6.4), whose chord coincides with the bottom side of the large square inclusion. In this case, all inclusions are in the “detectable region”, and hence all the boundaries are reconstructed sharply. The third column represents the full data reconstruction. Notice that the quality of the final reconstructions in the last two columns is the same. Figure 6.6a and b show the reconstructed image  $f(x)$  along the dashed-dotted line in Figure 6.4, using the FBP (Figures 6.5d through f) and TCG reconstructions (Figure 6.5g through i), respectively. The exact value is also shown for comparison. It can be found in Figure 6.6a that the results of FBP are in good agreement with the real value for the case of 217-degree and 360-degree detection, where all objects are in the “detectable region”. Iteration improves the results further, as shown in Figure 6.6b. Even for the case of a 90-degree detection curve, the profile of the objects is reconstructed. Comparing Figure 6.6a and b, one finds that the significant overshoot and undershoot in FBP can be considerably reduced by TCG iterations (we remind the reader that FBP is only an approximation rather than the implementation of an exact formula).

Figure 6.7 shows the relative error of each reconstruction as a function of the scanned angular range with respect to the center of the scan. We study the mean reconstruction values in the hard sphere, the central square, and the background. The errors of reconstruction are normalized to the corresponding real values in the cases of the hard sphere and the central square, and to the real value of the hard sphere in the case of the background (because its real value is zero). When the scanned angular range is less than  $\pi$ , the errors decrease sharply with increasing scanned angular range. By contrast, when the scanned angular range is larger than  $\pi$ , the errors change much more slowly as the scanned angular range increases. The results agree with our theoretical conclusions. However, there are some fluctuations added to the trends of the curves. By comparing the three curves in Figure 6.7, we find that these fluctuations depend strongly on the location of the object with respect to the detection curve. More extensive study is needed to understand these fluctuations. There are some residual errors even in the full-view detection in Figure 6.7. This is because we used an approximate backprojection algorithm, rather than an exact inversion (which was not available at that time).

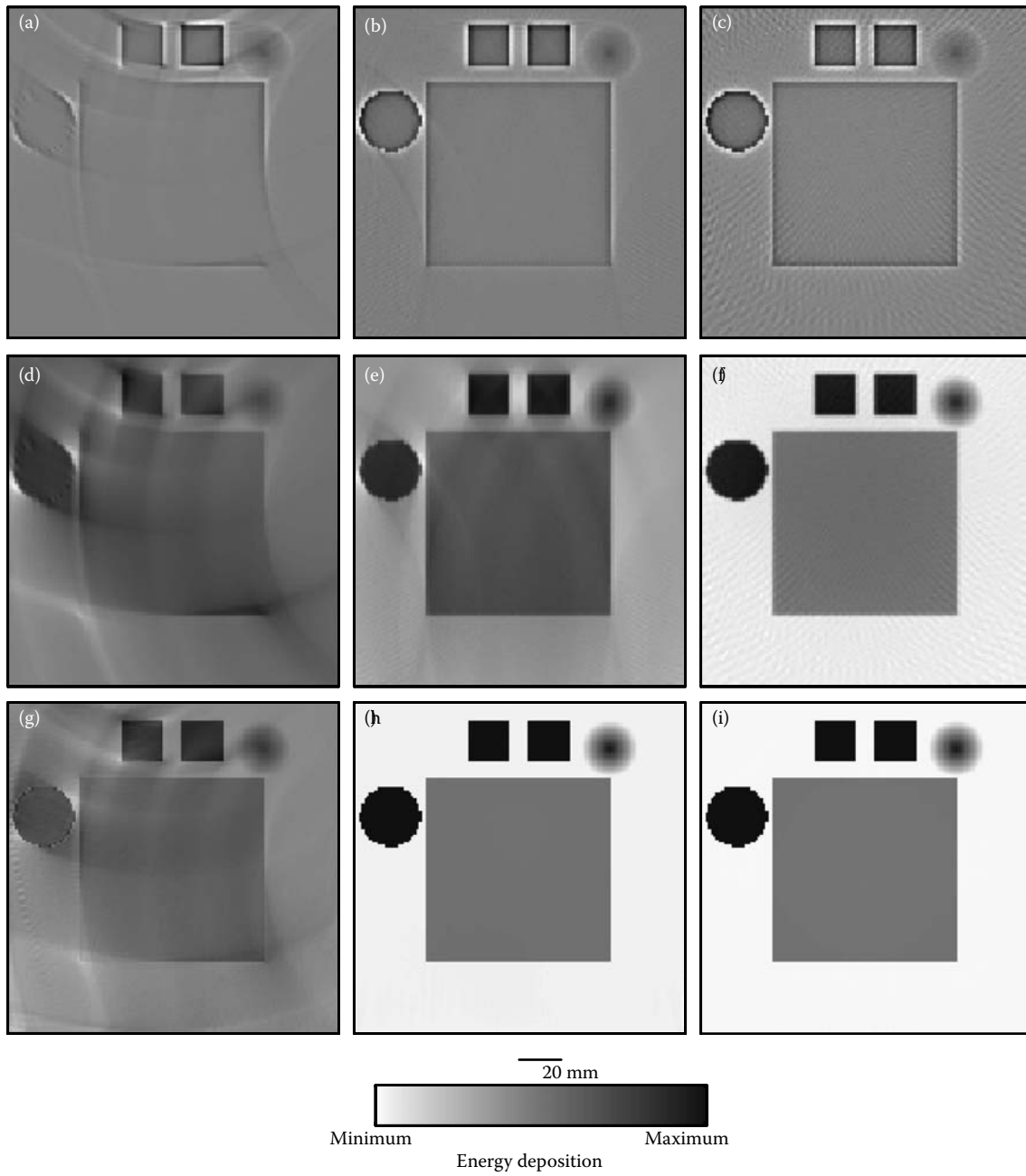


**FIGURE 6.5** Images reconstructed from simulated TAT data corresponding to the phantom in Figure 6.4. The three columns correspond from left to right to detection angles of 90 degrees (from 0° to 90°), 217 degrees (from -19° to 198° as shown by the angle  $\theta$  in Figure 6.4), and 360 degrees, respectively. The three rows correspond from top to bottom to the local tomographic reconstruction, FBP, and FBP with the consecutive TCG, respectively. The values (minimum, maximum) of the gray scale for (a–i) are (-0.8081, 1.0000), (-0.8302, 1.0000), (-0.7515, 1.0000), (-2.0745, 1.7899), (-0.6385, 1.0723), (-0.1030, 1.0349), (-0.9284, 1.2859), (-0.0326, 1.0030), and (-0.0149, 1.0021), respectively. The maxima of the local reconstructions are normalized to unity. (Reproduced from Xu, Y., L.V. Wang, G. Ambartsoumian, and P. Kuchment, *Med. Phys.* 31(4):724–33, 2005. With permission.)

#### 6.4.2 RECONSTRUCTION FROM EXPERIMENTAL LIMITED VIEW THERMOACOUSTIC TOMOGRAPHY DATA

The experimental setup is described in [23,67] and will not be repeated here. The sample and the polar coordinate system describing the scanning orbit are shown in Figure 6.8a. The sample consists of a muscle cylinder of 4 mm in diameter and 5 mm in length, embedded in a chunk of pork

fat of 1.2 cm in radius,  $r_f$ . There is a 10-mm fat layer below the muscle and another 7-mm one above it. An EM pulse is delivered to the sample from below (i.e., from behind the picture plane). With a scanning radius of  $r_d = 7.1$  cm, thermoacoustic data are collected around the sample over a  $2\pi$  angular span with 161 steps. The EM pulse profile and the impulse response function of the ultrasonic transducer impose a filter on the thermoacoustic signals. We

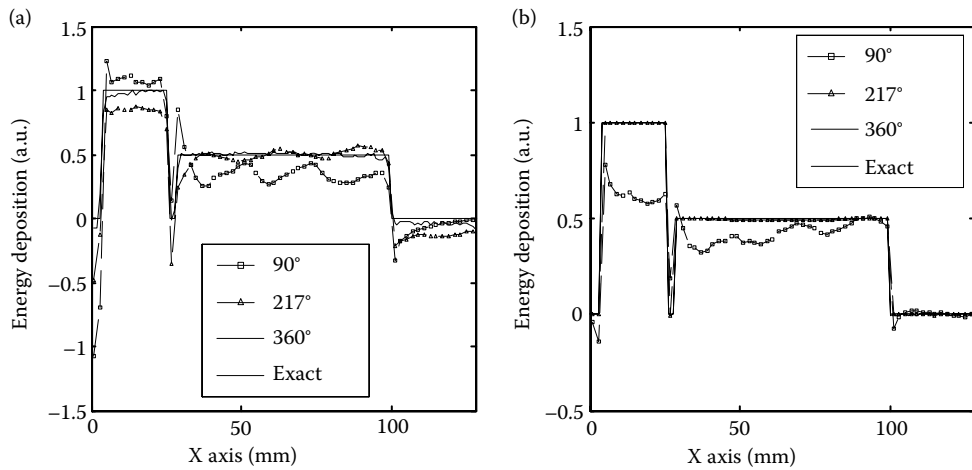


**FIGURE 6.6** (a) The graphs of FBP reconstructions shown in Figure 6.5d through f, and the corresponding exact value along the dashed-dotted line in Figure 6.4. (b) The graphs corresponding to TCG reconstructions, Figure 6.5d through f, along the same line as in (a). (Reproduced from Xu, Y., L.V. Wang, G. Ambartsoumian, and P. Kuchment, *Med. Phys.* 31(4):724–33, 2005. With permission.)

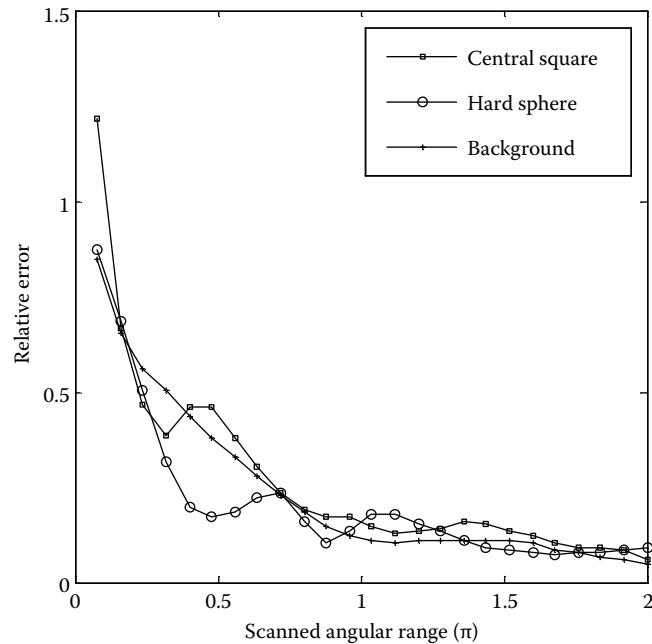


**FIGURE 6.7** Dependence of the relative errors of the mean values in the hard sphere (circle markers), the central square (square markers), and the background (asterisks) on the scanned angular range. (Reproduced from Xu, Y., L.V. Wang, G. Ambartsoumian, and P. Kuchment, *Med. Phys.* 31(4):724–33, 2005. With permission.)

attempted to correct this effect using deconvolution, but found that the resulting images were distorted, due to the lack of precise knowledge of the filter. Therefore, we do not use deconvolution in the reconstruction. This leads, as explained earlier, to somewhat emphasized interfaces. Figure 6.8b through d show the reconstructed images using FBP with three sets of data. In Figure 6.8b, we choose the data collected along a circular detection arc of 92 degrees, located at the top of the picture and almost symmetric with respect to its vertical axes. One sees that the left and right

boundaries of the muscle cylinder and of the pork chunk are blurred away, since their normal lines do not touch the detection arc, while the rest of the boundary is sharp. The next figure shows the reconstructed image obtained with the data collected from a 202-degree arc, where the whole phantom fits into the detectable region. All boundaries are sharp now. Finally, the last figure shows the image reconstructed with the full-view data.

Notice that although no local reconstruction algorithms are applied, the boundaries are somewhat emphasized. The reason for this is the presence in the data of the impulse response function of the ultrasonic transducer, which has an effect similar to the application of an additional derivative with respect to the radius of the circle of integration. The presence of such a derivative emphasizes high frequencies and makes the reconstruction similar to a version of a local tomography algorithm.

#### 6.4.3 DISCUSSION ON EXPERIMENTAL RESULTS

As mentioned earlier, although circular scanning is used in both our numerical and experimental studies, our conclusions can be applied to other configurations as well. In TAT with a planar configuration [62,64–66], detections are implemented on a part of a line or a plane where the scanning view is quite limited; consequently, artifacts and interface blurring appear in the reconstructed images. In fact, in planar and linear scanning geometries, one can never have an object immersed entirely into the “detectable region” because the normal lines to any interfaces that are orthogonal to the detection plane (line) never pass through a detector. As a consequence, those parts of the interfaces will be blurred in any kind of reconstruction. For a sufficiently large view, these parts will be small, but theoretically will never disappear. For example, 2D planar detection is utilized to image artificial blood vessels [64]; the scanning view is about 2.18 steradians. Therefore, it is not surprising that only the interfaces more-or-less parallel

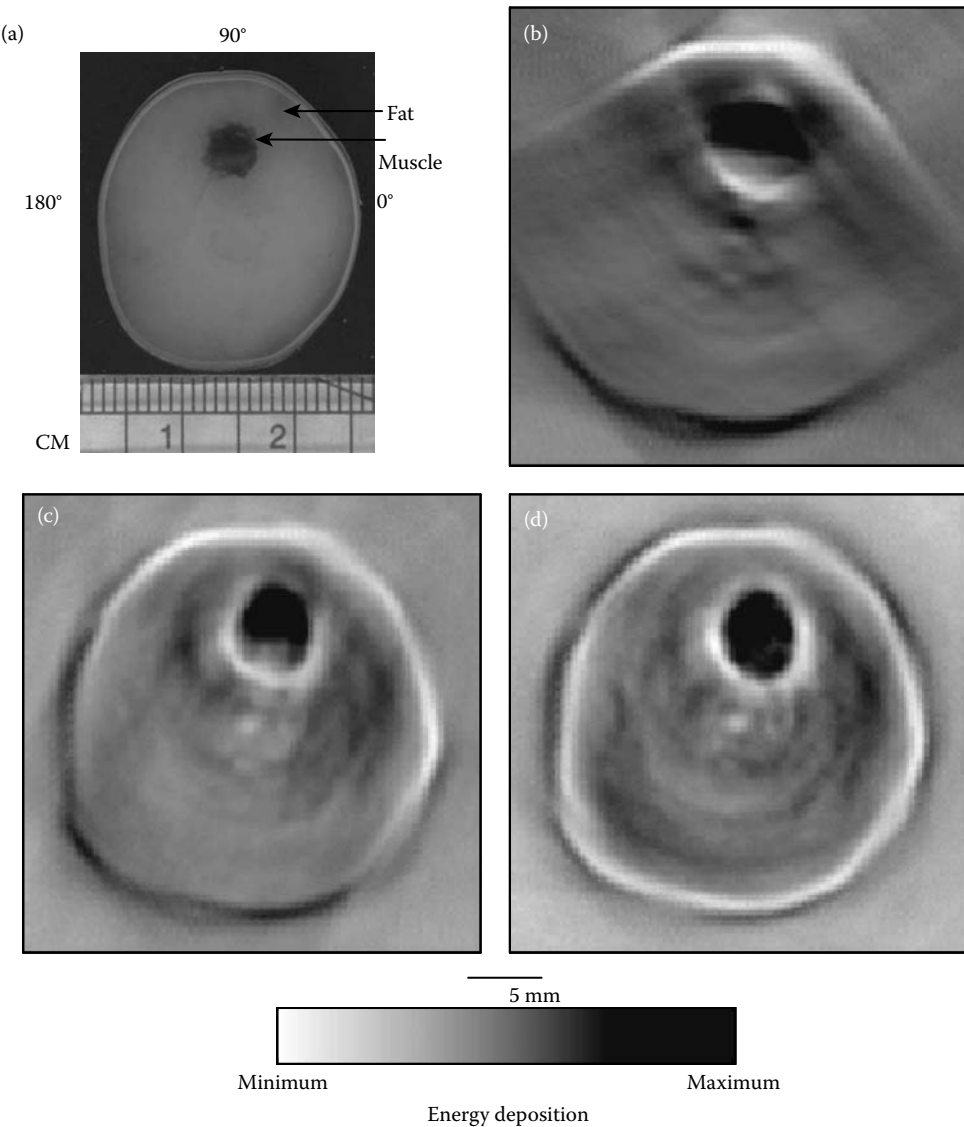


**FIGURE 6.8** (a) Photograph of the experimental sample. (b–d) TAT images reconstructed using detection arcs of 92 degrees (from  $50^\circ$  to  $142^\circ$  in (a)), 202 degrees (from  $-18^\circ$  to  $184^\circ$ ), and 360 degrees, respectively. The blurred parts of the boundaries in (b) due to the limited view agree with the theoretical predictions. In (c) all the boundaries are resolved, since the object fits into the “detectable region”. (Reproduced from Xu, Y., L.V. Wang, G. Ambartsoumian, and P. Kuchment, *Med. Phys.* 31(4):724–33, 2005. With permission.)

to the plane of detection are well imaged. Linear scanning detection was used in Ref. [66] to image a 2D phantom. Because the view of the linear scanning in Ref. [66] is much larger than that of planar scanning in Ref. [64], the interfaces are recovered much more completely. However, due to a limited view, artifacts and interface blurring similar to those demonstrated in our numerical and experimental studies still appear in the images [66].

By comparing Figures 6.5 and 6.8, we observe that the images reconstructed from incomplete data when an object is in the detectable region, have comparable quality with those from the full-view data. Scanning a smaller range has the advantages of reducing the scanning time or the size of the acoustic transducer array. It should be pointed out that this advantage usually exists when both the sample and medium are relatively acoustically homogeneous. When

strong wavefront distortion caused by acoustic heterogeneities occurs, it might be beneficial to collect signals from all directions.

## 6.5 ADDITIONAL REMARKS AND CONCLUSIONS

As mentioned before, one may incorporate some additional information about the image, or change the physical set-up of the problem to stabilize the inverse problem and make all or some formerly invisible interfaces visible. Recently, it was shown [70] that taking into account some *a priori* knowledge about the interfaces leads to reconstruction of previously invisible parts. In another direction, acoustic reflectors were proposed as a means of reflecting the acoustic waves, which would otherwise not be measured, back onto the sensor. It was

shown in that case an existing FFT-based image reconstruction algorithm can be used to reconstruct the image without the limited view-induced blurring [71,81].

The main points of this survey can be summarized as follows:

- A geometric principle is described that allows a simple determination of which sharp parts of the object are expected to be blurred when reconstructed from limited view thermoacoustic data.
- This blurring is independent of the particular reconstruction method and cannot be overcome, unless some extra information about the object is known.
- Numerical results using synthetic and experimental data are shown that support the conclusions.

## ACKNOWLEDGMENTS

The work of Y.X. was supported in part by Ryerson University and NSERC discovery grant, L.W. was supported in part by NIH grants R01 NS46214 and R01 EB000712, G.A. was supported by the DOD grant BC063989 and the grant REP-GCS07457 of the University of Texas at Arlington, and P.K. was partially supported by the NSF DMS grants 0604778 and 0648786. The authors express their gratitude to M. Anastasio, P. Burkholzer, D. Finch, L. Kunyansky, and G. Paltauf for information and discussions.

## REFERENCES

1. Joines, W.T. 1980. Microwave-power absorption differences between normal and malignant-tissue. *Int. J. Radiat. Oncol. Biol. Phys.* 6:681–87.
2. Chaudhary, S.S. 1984. Dielectric-properties of normal and malignant human-breast tissues at radiowave and microwave-frequencies. *Indian J. Biochem. Biophys.* 21:76–79.
3. Joines, W.T., Y. Zhang, C.X. Li, and R.L. Jirtle. 1994. The measured electrical-properties of normal and malignant human tissues from 50 to 900 MHz. *Med. Phys.* 21(4): 547–50.
4. Cheong, W.F., S.A. Prahl, and A.J. Welch. 1990. A review of the optical-properties of biological tissues. *IEEE J. Quantum Electron.* 26 (12):2166–85.
5. Kruger, R.A., P.Y. Liu, Y.R. Fang, and C.R. Appledorn. 1995. Photoacoustic ultrasound (PAUS)—reconstruction tomography. *Med. Phys.* 22 (10):1605–609.
6. Oraevsky, A.A., and A.A. Karabutov. 2002. In *Handbook of optical biomedical diagnostics*, ed. V.V. Tuchin, Chap. 10. Bellingham, WA: SPIE.
7. Oraevsky, A.A., and A.A. Karabutov. 2003. Optoacoustic tomography. In *Biomedical photonics handbook*, ed. T. Vo-Dinh, Chap. 34. Boca Raton, FL: CRC.
8. Wang, L.V., and H. Wu. 2007. *Biomedical optics. Principles and imaging*. New York: Wiley-Interscience.
9. Xu, M., and L.-H. V. Wang. 2006. Photoacoustic imaging in biomedicine. *Rev. Sci. Instrum.* 77:041101-01–22.
10. Natterer, F. 1986. *The mathematics of computerized tomography*. New York: Wiley.
11. Quinto, E.T. 1993. Singularities of the x-ray transform and limited data tomography in  $R(2)$  and  $R(3)$ . *SIAM J. Math. Anal.* 24(5):1215–25.
12. Ramm, A.G., and A.I. Zaslavsky. 1993. Reconstructing singularities of a function from its Radon Transform. *Math. Comput. Modelling* 18(1):109–38.
13. Delaney, A.H., and Y. Bresler. 1998. Globally convergent edge-preserving regularized reconstruction: An application to limited-angle tomography. *IEEE Trans. Image Processing* 7(2):204–21.
14. Pan, X.C., and M.A. Anastasio. 1999. Minimal-scan filtered backpropagation algorithms for diffraction tomography. *J. Opt. Soc. Am. A* 16(12):2896–2903.
15. Kuchment, P., and E.T. Quinto. 2003. Some problems of integral geometry arising in tomography, Chapter XI in L. Ehrenpreis *The universality of the radon transform*. Oxford: Oxford University Press.
16. Natterer, F., and F. Wübbeling. 2001. *Mathematical methods in image reconstruction*. Philadelphia, PA: SIAM.
17. Pan, X.C., Y. Zou, and M.A. Anastasio. 2003. Data redundancy and reduced-scan reconstruction in reflectivity tomography. *IEEE Trans. Image Processing* 12(7):784–95.
18. Kuchment, P., K. Lancaster, and L. Mogilevskaya. 1995. On local tomography. *Inverse Problems* 11(3):571–89.
19. Louis, A.K., and E.T. Quinto. 2000. Local tomographic methods in Sonar. In *Surveys on solution methods for inverse problems*, eds. D. Colton, H. Engl, A. Louis, J. McLaughlin, and W. Rundell, 147–54. Vienna: Springer.
20. Palamodov, V.P. 2000. Reconstruction from limited data of arc means. *J. Fourier Anal. Appl.* 6(1):25–42.
21. Patch, S.K. 2000. Moment conditions indirectly improve image quality. *Contemp. Math.* 278:193–205.
22. Patch, S.K. 2004. Thermoacoustic tomography – consistency conditions and the partial scan problem. *Phys. Med. Biol.* 49:1–11.
23. Xu, Y., L.V. Wang, G. Ambartsoumian, and P. Kuchment. 2004. Reconstructions in limited-view thermoacoustic tomography. *Med. Phys.* 31(4):724–33.
24. Paltauf, G., R. Nuster, M. Haltmeier, and P. Burgholzer. 2007. Experimental evaluation of reconstruction algorithms for limited view photoacoustic tomography with line detectors. *Inverse Problems* 23:S81–S94.
25. Paltauf, G., R. Nuster, P. Burgholzer, and M. Haltmeier. 2007. Three-dimensional photoacoustic tomography (PAT) using optical line detection of ultrasound. Lecture at the Workshop on Bioimaging, Johann Radon Institute for Computational and Applied Mathematics, Linz, Austria, 12–17 November.
26. Andreev, V., D. Sushko, A. Oraevsky, A. Karabutov, and D. Popov. 2002. Image reconstruction in 3D optoacoustic tomography system with hemispherical transducer array. *Proc. SPIE* 4618:1605–7422/02.
27. Anastasio, M.A., J. Zhang, E.Y. Sidky, Y. Zou, D. Xia, and X. Pan. 2005. Feasibility of half-data image reconstruction in 3-D reflectivity tomography with a spherical aperture. *IEEE Trans. Med. Imaging* 24(9):1100–12.
28. Finch, D., and Rakesh. 2007. The spherical mean value operator with centers on a sphere. *Inverse Problems* 23(6):S37–S50.
29. Patch, S.K., and O. Scherzer. 2007. Photo- and thermoacoustic imaging. *Inverse Problems* 23(6):S1–S10.
30. Kuchment, P., and L. Kunyansky. 2008. Mathematics of thermoacoustic tomography. *Eur. J. Appl. Math.* 19(2):191–224.
31. Agranovsky, M., P. Kuchment, and L. Kunyansky. 2009. On reconstruction formulas and algorithms for the thermoacoustic and photoacoustic tomography. In *Photoacoustic Imaging and Spectroscopy*, ed. Lihong Wang, 89–102, Boca Raton, FL: CRC press.

32. Finch, D., and Rakesh. 2009. Recovering a function from its spherical mean values in two and three dimensions. In *Photoacoustic Imaging and Spectroscopy*, ed. Lihong Wang, 77–88, Boca Raton, FL: CRC press.
33. Arfken, G.B., and H.J. Weber. 2005. *Mathematical methods for physicists*. New York: Academic Press.
34. Courant, R., and D. Hilbert. 1962. *Methods of mathematical physics, Volume II Partial differential equations*. New York: Wiley-Interscience.
35. Agranovsky, M.L., and E.T. Quinto. 1996. Injectivity sets for the Radon transform over circles and complete systems of radial functions. *J. Funct. Anal.* 139(2):383–414.
36. Xu, Y., and L.H.V. Wang. 2004. Time reversal and its application to tomography with diffracting sources. *Phys. Rev. Lett.* 92(3):4.
37. Xu, Y., and L.H.V. Wang. 2004. Time reversal and its application to thermoacoustic tomography. *Proc. SPIE* 5320:257–63.
38. Finch, D., S. Patch, and Rakesh. 2004. Determining a function from its mean values over a family of spheres. *SIAM J. Math. Anal.* 35(5):1213–40.
39. Palamodov, V.P. 2004. *Reconstructive integral geometry*. Basel: Birkhäuser.
40. Ambartsoumian, G., and Kuchment, P. 2005. On the injectivity of the circular Radon transform. *Inverse Problems* 21:473–85.
41. Kuchment, P. 2006. Generalized transforms of radon type and their applications. In *The Radon Transform, Inverse Problems, and Tomography*. American Mathematical Society Short Course January 3–4, 2005, Atlanta, Georgia, eds. G. Olafsson and E.T. Quinto, 67–91. Proc. Symp. Appl. Math., v. 63, Providence, RI: AMS.
42. Agranovsky, M., P. Kuchment, and E.T. Quinto. 2007. Range descriptions for the spherical mean Radon transform, *J. Funct. Anal.* 248:344–86.
43. Agranovsky, M., and P. Kuchment. 2007. Uniqueness of reconstruction and an inversion procedure for thermoacoustic and photoacoustic tomography. *Inverse Problems* 23:2089–102.
44. Kuchment, P. 1993. Unpublished.
45. Agranovsky, M., C. Berenstein, and P. Kuchment. 1996. Approximation by spherical waves in  $L_p$ -spaces. *J. Geom. Anal.* 6(3):365–83.
46. Fawcett, J.A. 1985. Inversion of n-dimensional spherical averages. *SIAM J. Appl. Math.* 45:336–41.
47. Andersson, L.E. 1988. On the determination of a function from spherical averages. *SIAM J. Math. Anal.* 19:214–32.
48. Nilsson, S. 1997. Application of fast backprojection techniques for some inverse problems of integral geometry, PhD thesis, Linkoping University, Linkoping.
49. Denisjuk, A. 1999. Integral geometry on the family of semi-spheres. *Fract. Calc. Appl. Anal.* 2:31–46.
50. Xu, Y., D.Z. Feng, and L.H.V. Wang. 2002. Exact frequency-domain reconstruction for thermoacoustic tomography – I: Planar geometry. *IEEE Trans. Med. Imaging* 21(7):823–28.
51. Norton, S.J. 1980. Reconstruction of a two-dimensional reflecting medium over a circular domain: Exact solution. *J. Acoust. Soc. Am.* 67:1266–73.
52. Norton, S.J., and M. Linzer. 1981. Ultrasonic reflectivity imaging in three dimensions: Exact inverse scattering solution for plane, cylindrical and spherical aperture. *IEEE Trans. Biomed. Eng.* BME-28:202–20.
53. Finch, D., M. Haltmeier, and Rakesh. 2007. Inversion of spherical means and the wave equation in even dimensions. *SIAM J. Appl. Math.* 68(2), 392–412.
54. Xu, M., and L.-H.V. Wang. 2005. Universal back-projection algorithm for photoacoustic computed tomography. *Phys. Rev. E* 71:016706.
55. Kunyansky, L. 2007. Explicit inversion formulae for the spherical mean Radon transform. *Inverse Problems* 23:373–83.
56. Rubin, B. 2007. Spherical means in odd dimensions and EPD equations. Preprint arXiv:arXiv:0711.1897.
57. Kunyansky, L. 2007. A series solution and a fast algorithm for the inversion of the spherical mean Radon transform. *Inverse Problems* 23(6):S11–S20.
58. Popov, D.A., and D.V. Sushko. 2002. A parametrix for the problem of optical-acoustic tomography. *Dokl. Math.* 65(1):19–21.
59. Popov, D.A., and D.V. Sushko. 2004. Image restoration in optical-acoustic tomography. *Problems Inform. Transmission* 40(3):254–78.
60. Burgholzer, P., G. Matt, M. Haltmeier, and G. Paltauf. 2007. Exact and approximate imaging methods for photoacoustic tomography using an arbitrary detection surface. *Phys. Rev. E* 75:046706.
61. Hristova, Y., P. Kuchment, and L.V. Nguyen. 2008. On reconstruction and time reversal in thermoacoustic tomography in acoustically homogeneous and inhomogeneous media. *Inverse Problems* 24:055006.
62. Hoelen, C.G.A., F.F.M. de Mul, R. Pongers, and A. Dekker. 1998. Three-dimensional photoacoustic imaging of blood vessels in tissue. *Opt. Lett.* 23(8):648–50.
63. Kostli, K.P., M. Frenz, H. Bebie, and H.P. Weber. 2001. Temporal backward projection of optoacoustic pressure transients using Fourier transform methods. *Phys. Med. Biol.* 46(7):1863–72.
64. Hoelen, C.G.A., and F.F.M. de Mul. 2000. Image reconstruction for photoacoustic scanning of tissue structures. *Appl. Opt.* 39(31):5872–83.
65. Ku, G., and L.H.V. Wang. 2001. Scanning microwave-induced thermoacoustic tomography: Signal, resolution, and contrast. *Med. Phys.* 28(1):4–10.
66. Feng, D.Z., Y. Xu, G. Ku, and L.V. Wang. 2001. Microwave-induced thermoacoustic tomography: Reconstruction by synthetic aperture. *Med. Phys.* 28(12):2427–31.
67. Xu, M.H., and L.H.V. Wang. 2002. Time-domain reconstruction for thermoacoustic tomography in a spherical geometry. *IEEE Trans. Med. Imaging* 21(7):814–22.
68. Xu, Y., M.H. Xu, and L.H.V. Wang. 2002. Exact frequency-domain reconstruction for thermoacoustic tomography - II: Cylindrical geometry. *IEEE Trans. Med. Imaging* 21(7):829–33.
69. Haltmeier, M., T. Schuster, and O. Scherzer. 2005. Filtered backprojection for thermoacoustic computed tomography in spherical geometry. *Math. Methods Appl. Sci.* 28:1919–37.
70. Wang, L.H.V., and X.M. Yang. 2007. Boundary conditions in photoacoustic tomography and image reconstruction. *J. Biomed. Opt.* 12(1):10.
71. Cox, B.T., and P.C. Beard. 2007. Exact photoacoustic image reconstruction using a planar sensor array and image sources. *SPIE* 6437:64371H.
72. Strichartz, R.S. 2003. *A guide to distribution theory and Fourier transforms*. Singapore: World Science.

73. Quinto, E.T. 1980. The dependence of the generalized Radon transform on defining measures. *Trans. Am. Math. Soc.* 257:331–46.
74. Beylkin, G. 1984. The inversion problem and applications of the generalized radon-transform. *Commun. Pure Appl. Math.* 37:579–99.
75. Noo, F., and J.-M. Wagner. 2001. Image reconstruction in 2D SPECT with 180° acquisition. *Inverse Problems* 17:1357–71.
76. Rullgård, H. 2004. An explicit inversion formula for the exponential Radon transform using data from 180°. *Ark. Mat.* 4(2):353–62.
77. Kunyansky, L. 2008. Thermoacoustic tomography with detectors on an open curve: an efficient reconstruction algorithm. *Inverse Problems* 24(5):055021.
78. Faridani, A., E.L. Ritman, and K.T. Smith. 1992. Examples of local tomography. *SIAM J. Appl. Math.* 52(4):1193–98.
79. Faridani, A., E.L. Ritman, and K.T. Smith. 1992. Local tomography. *SIAM J. Appl. Math.* 52(2):459–84.
80. Faridani, A., D.V. Finch, E.L. Ritman, and K.T. Smith. 1997. Local tomography. 2. *SIAM J. Appl. Math.* 57(4): 1095–1127.
81. Cox, B.T., S.R. Arridge, and P.C. Beard. 2007. Photoacoustic tomography with a limited-aperture planar sensor and a reverberant cavity. *Inverse Problems* 23:S95–S112.